

# 1 Predicting Deep-Seated Landslide Displacements in Lushan Mountain through the Integration 2 of Convolutional Neural Networks and an Age of Exploration-Inspired Optimizer

3 Jui-Sheng Chou<sup>1,\*</sup>, Hoang-Minh Nguyen<sup>1</sup>, Huy-Phuong Phan<sup>1</sup>, Kuo-Lung Wang<sup>2</sup>

4 <sup>1</sup>Department of Civil and Construction Engineering, National Taiwan University of Science and Technology, Taipei, Taiwan

5 <sup>2</sup>Department of Civil Engineering, National Chi Nan University, Nantou, Taiwan

6 ([jschou@mail.ntust.edu.tw](mailto:jschou@mail.ntust.edu.tw); [hoangminhkg1992@gmail.com](mailto:hoangminhkg1992@gmail.com); [huyphuong777@gmail.com](mailto:huyphuong777@gmail.com); [klwang@ncnu.edu.tw](mailto:klwang@ncnu.edu.tw))

7 \*Correspondence e-mail address: [jschou@mail.ntust.edu.tw](mailto:jschou@mail.ntust.edu.tw)

## 8 Abstract

9 Deep-seated landslides have caused substantial damage to both human life and infrastructure in the past.  
10 Developing an early warning system for this type of disaster is crucial to reduce its impact on society.  
11 This research contributes to developing predictive early warning systems for deep-seated slope  
12 displacements by employing advanced computational models for environmental risk management. Our  
13 novel framework integrates machine learning, time series deep learning, and convolutional neural  
14 networks (CNN), enhanced by the Age of Exploration-Inspired Optimizer (AEIO) algorithm. Our  
15 approach demonstrates exceptional forecasting capabilities by utilizing eight years of comprehensive  
16 data—including displacement, groundwater levels, and meteorological information from the Lushan  
17 Mountain region in Taiwan. The AEIO-MobileNet model precisely predicts imminent slope  
18 displacements with a mean absolute percentage error (MAPE) of 2.81%. These advancements  
19 significantly enhance geohazard informatics by providing reliable and efficient landslide risk assessment  
20 and management tools. These safeguard road networks, construction projects, and infrastructure within  
21 vulnerable slope areas.

22 **Keywords:** deep-seated landslide; displacement forecasting; landslide risk assessment; early warning  
23 system; machine learning; time-series deep learning; convolutional neural network; metaheuristic  
24 optimization.

## 25 1. Introduction

26 Landslides are among the most devastating natural disasters (Huang and Fan, 2013), claiming an  
27 average of over 4,000 lives annually worldwide between 2004 and 2010 (Petley, 2012). Landslides  
28 represent a global hazard, particularly in developing countries, where rapid urbanization, population  
29 growth, and significant land use changes occur (Caleca et al., 2024). The identification, management, and  
30 monitoring of landslides are made difficult by the diversity of their types (shallow slides, deep-seated  
31 slides, rock falls, rock slides, debris flows) and the complexity of their categorization based on triggers,  
32 material composition, movement speed, and other characteristics (Das et al., 2022; Hungr et al., 2014).  
33 These issues are further exacerbated in countries with complex geological and climatic conditions.

34 A deep-seated landslide involves the gradual and persistent displacement of a substantial amount of  
35 soil and rock, which can escalate into a sudden and devastating event (Kilburn and Petley, 2003;  
36 Geertsema et al., 2006; Chigira, 2009). Unlike shallow landslides, which typically affect surface layers to  
37 a few meters, deep-seated landslides extend deeper, often exceeding 10 meters, and can involve the  
38 movement of underlying bedrock (Lin et al., 2013). Predicting these events is challenging and costly (Thai  
39 Pham et al., 2019). Therefore, extensive efforts have been made to predict such disasters throughout  
40 history. One method that has been employed involves thoroughly examining the physical and geological  
41 characteristics of the mountainous areas at risk of landslides (Cotecchia et al., 2020). Furthermore, the  
42 level of groundwater has been shown by numerous studies in the past to influence the mechanisms behind  
43 landslide formation significantly (Miao and Wang, 2023; Preisig, 2020).

44 In pursuing a generalized approach to landslide forecasting, researchers have determined that the  
45 critical factors associated with slope instability exhibit temporal variability, necessitating using time series  
46 data (Chae et al., 2017). This approach combines slope deformation data collected through sensors drilled  
47 deep into the slope bed with data on the natural conditions of the monitoring area, which is collected  
48 simultaneously. Upon establishing that the data pertinent to landslide prediction falls within the category  
49 of time series data, a formidable challenge in research related to this type of disaster is devising a predictive  
50 model capable of forecasting the likelihood of such catastrophes based on related factors.

51 One of the most effective solutions for constructing models to predict time series data involves  
52 applying data-driven techniques. The advancement of computational capabilities has driven the  
53 widespread adoption of data-driven machine-learning models over physics-based models. This shift is  
54 based on the premise that the data used for slope monitoring originates from nonlinear systems (Zhou et  
55 al., 2018). An increasing array of novel data-driven solutions is being developed to overcome the  
56 constraints of traditional machine-learning approaches. Among these data-driven solutions, convolutional  
57 neural networks (CNN) have emerged as one of the most effective methods. These CNN models, which  
58 excel at automated feature extraction, can enhance efficiency in analyzing complex datasets and improve  
59 the accuracy of prediction results (Alzubaidi et al., 2021).

60 Moreover, there is a noteworthy recent trend in employing metaheuristic optimization algorithms to  
61 fine-tune the hyperparameters of artificial intelligence (AI) models, thereby augmenting their efficiency.  
62 This approach has found application in geological and construction studies and other fields, showcasing  
63 substantial effectiveness. Consequently, the fine-tuning of hyperparameters represents a potent avenue for  
64 elevating the efficiency of AI models in research focused on predicting deep-seated displacements.

65 Leveraging the effective methodologies mentioned above, this study employs AI models optimized  
66 by an innovative metaheuristic optimization algorithm to predict deep-seated displacement on the northern  
67 slope of Lushan Mountain in Ren'ai Township, Nantou County. The geological characteristics of this area

68 have undergone extensive research (Wang et al., 2015; Lin et al., 2020). Previous studies have identified  
69 varying depths of the shear plane. Specifically, Lin et al. (2020) determined the depth of the shear plane  
70 is 85m and 106m based on inclinometer data. This research paper is firmly grounded in empirical evidence  
71 meticulously collected over eight years from extensometers at depths of 70 and 40 meters. Our analysis  
72 also considers the cumulative impact of storms and heavy rainfall on groundwater levels, utilizing data  
73 from four stations measuring groundwater levels in the study area and other weather conditions that  
74 potentially trigger landslides. The objectives of our research were as follows:

- 75 1) To analyze the application of machine learning and deep learning methods to time series data to forecast  
76 short-term, deep-seated slope displacements across the Lushan Mountain area.
- 77 2) To identify the optimal model and hyperparameters for accurately forecasting deep-seated  
78 displacements in the study area.
- 79 3) To evaluate the role of metaheuristic optimization algorithms in fine-tuning the hyperparameters of AI  
80 models.

81 This study represents the first instance of AI models being utilized to predict deep-seated landslides  
82 in Lushan Mountain. Additionally, it marks the inaugural application of AEIO for fine-tuning AI models  
83 in landslide-related research. Our findings provide a valuable resource for civil engineers, contractors, and  
84 inspectors involved in the planning and monitoring of construction projects in landslide-prone areas.  
85 Predicting the likelihood of landslide events can help minimize property loss, guide schedule adjustments,  
86 improve work safety, and ensure smooth traffic flow during critical periods. Additionally, understanding  
87 internal displacements provides engineers with precise data to evaluate the resilience of structures and  
88 infrastructure in vulnerable areas, enabling the issuance of prudent warnings.

## 89 **2. Literature Review**

### 90 **2.1 Groundwater Levels and the Forecasting of Deep-Seated Displacements**

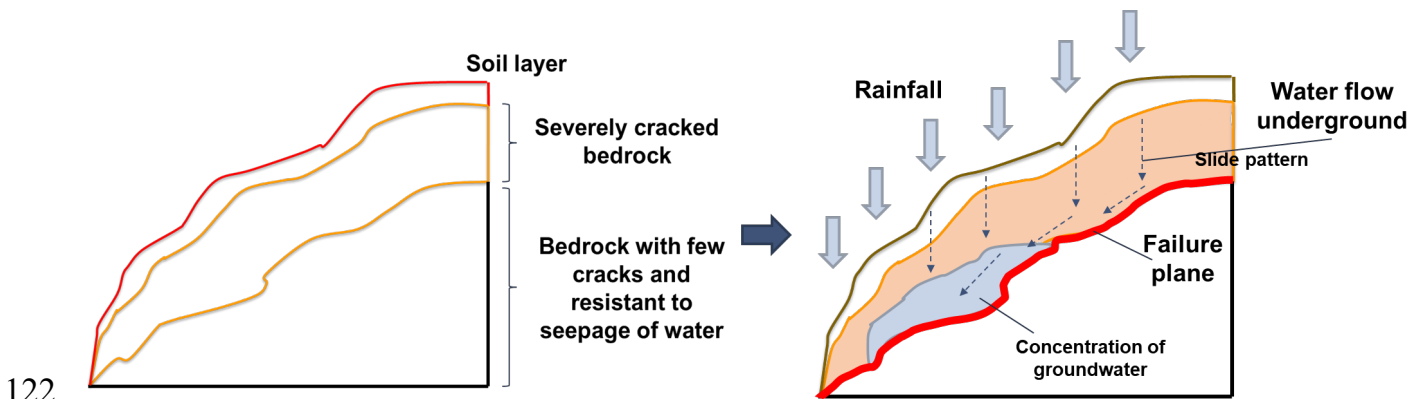
91 Landslide triggers can be attributed to loading, slope geometry, weather conditions, and  
92 hydrological conditions (Perkins et al., 2024; Van Natijne et al., 2023; Millán-Arancibia and Lavado-  
93 Casimiro, 2023; Jones et al., 2023). Among these, hydrological conditions, especially groundwater levels,  
94 have been one of the most critical elements considered in studies related to landslide prediction. Numerous  
95 studies have substantiated this point. For instance, research by Take et al. (2015) demonstrated that the  
96 distance and velocity of landslides triggered under high-antecedent groundwater conditions are  
97 significantly more significant compared to scenarios with drier conditions. Another study has shown that  
98 water accumulation at a soil-bedrock contact can develop positive pore water pressures, causing landslides  
99 (Matsushi and Matsukura, 2007) (see Figure 1). Moreover, studies on past landslide events have also  
100 demonstrated similar findings. Examples of this research include the Tessina landslide in northeastern  
101 Italy, where groundwater conditions triggered movement (Petley et al., 2005). Additionally, the study by

102 Keqiang et al. (2015) on water-induced landslides in the Three Gorges Reservoir project area highlights  
103 the significant impact of hydrological conditions on the likelihood of such disasters.

104 Similarly, Preisig (2020) developed a groundwater prediction model for analyzing the stability of a  
105 compound slide in the Jura Mountains. Additionally, Srivastava et al. (2020) explored machine learning  
106 algorithms to forecast rainfall and established thresholds for landslide probabilities. Although the research  
107 by Srivastava et al. did not directly rely on groundwater levels to predict landslides, it is evident that  
108 rainfall, a crucial factor in their study for landslide prediction, also influences hydrological conditions.  
109 Therefore, their research further underscores the importance of considering groundwater levels in  
110 landslide prediction.

111 The northern slope in the Lushan area of central Taiwan, the region investigated in this study,  
112 exhibits significant gravitational slope deformation, making it prone to landslides during typhoons or  
113 heavy rainfall events. Lin et al. (2020) conducted in-depth studies on the mechanisms of landslide  
114 occurrence based on the geological conditions of the area. While successfully providing valuable insights  
115 into the evolution of deep-seated gravitational deformations, their study focuses exclusively on employing  
116 traditional analytical methods in geological research, such as analyzing data from geotechnical  
117 instruments and conducting geological borehole analysis.

118 Our research aims to adopt a novel approach compared to previous landslide studies at Lushan  
119 Mountain by utilizing AI models and metaheuristic optimization algorithms. This research will utilize  
120 weather conditions and groundwater levels as inputs for AI models to predict deep-seated displacement,  
121 thus aiding in landslide forecasting in this region.



123 Figure 1. Schematic illustration showing the effects of groundwater on deep-seated slope failure

## 124 2.2 Forecasting Slope Displacements: Conventional Methods

125 Several conventional methods are commonly employed to predict deep slope displacement. These  
126 methods primarily involve simulating factors affecting slope stability in landslide-prone areas using data  
127 collected from ground-based monitoring devices. An early approach to predicting deep-seated slope  
128 movements is geotechnical mapping. This technique characterizes rock and soil's strength, density, and  
129 porosity.

130 For instance, Crosta and Agliardi (2003) analyzed the geology and rock mass behavior using  
131 Voight's semi-empirical failure criterion, incorporating time-dependent factors to generate velocity curves  
132 that indicate risk levels. Recently, Xu et al. (2018) utilized real-time remote monitoring systems to  
133 measure internal stress, deep displacement, and surface strain. This data was used to formulate forecasting  
134 models to assess slope stability, particularly in railway construction. However, a common challenge with  
135 this method is the instability and frequent changes in the terrain and geology of landslide-prone areas.  
136 This necessitates constant updates to the computational model, which can be time-consuming and labor-  
137 intensive.

138 Moreover, physical-based numerical and laboratory modeling methods are also gaining traction in  
139 landslide research. These methods aim to maintain forecasts using various data types while reducing  
140 human workload and ensuring high accuracy. For example, Mufundirwa et al. conducted a laboratory  
141 study to examine the effectiveness of the inverse velocity model in predicting rock mass destruction  
142 resulting from landslides at depths of 2m and 4m along the sliding plane. This study utilized historically  
143 recorded data from Asamushi, Japan, and the Vaiont reservoir in Italy (Mufundirwa et al., 2010).  
144 Meanwhile, Wu (2010) employed the numerical discontinuous deformation analysis method to simulate  
145 a blocky assembly's post-failure behavior, incorporating earthquake seismic data. Another study follows  
146 this trend by Jiang et al. (2011), who utilized the fluid-solid coupling theory to simulate displacement and  
147 capture the interaction between fluid and solid materials. However, both numerical models and laboratory  
148 modeling methods require substantial effort from researchers. These approaches demand deep expertise  
149 and the development of complex models. More importantly, they rely heavily on assumptions during the  
150 simulation process and may not accurately reflect real-world conditions, leading to significant errors.

151 Stability analysis is another commonly used method related to physics, which evaluates the forces  
152 acting on a slope behavior. Fu and Liao (2010) presented a technique for implementing the non-linear  
153 Hoek-Brown shear strength reduction, determining the correlation between normal and shear stress based  
154 on the Hoek-Brown criterion. Subsequently, the micro-units (microscopic components of the rock mass)  
155 instantaneous friction angle and cohesive strength under specific stress conditions are calculated.  
156 Although this approach effectively addresses cost and labor issues, it still heavily relies on the researcher's  
157 assumptions and is limited by the ability to utilize only a small portion of data from the research area.

158 However, in landslide studies, monitoring data is constantly updated, generating large volumes daily  
159 with a temporal relationship (Peternel et al., 2022; Corominas et al., 2014). As previously mentioned,  
160 using conventional methods in landslide research presents numerous challenges whenever data changes  
161 or gets updated. In contrast, AI models can overcome these difficulties by automatically learning to  
162 identify connections between input and output data. AI models can be updated to incorporate additional

163 input variables and handle increasing amounts of data flexibly in response to real-world conditions.  
164 Therefore, AI models will be utilized in this research instead of conventional methods.

### 165 **2.3 Forecasting Slope Displacements: Machine Learning and Deep Learning**

166 In studies employing machine learning and deep learning models for landslide research, a plethora  
167 of research utilizes discrete data to train AI models to predict the probability of landslides or to construct  
168 maps depicting landslide susceptibility. For instance, Margarint et al. (2013) employed a logistic  
169 regression model to predict landslides based on discrete data in four regions of Romania. The logistic  
170 regression model yielded promising predictions, with an AUC value (area under the curve) ranging  
171 between 0.851 and 0.94 for the validation dataset. Subsequently, these results were utilized to construct a  
172 map of landslide susceptibility in the study area. In a similar study, Pham et al. (2016) used multiple AI  
173 models, including support vector machines (SVM), logistic regression (LR), Fisher's linear discriminant  
174 analysis (FLDA), Bayesian network (BN), and naïve Bayes (NB), for landslide susceptibility assessment  
175 in a region within the Uttarakhand state of India. The SVM model yielded the best prediction results  
176 among the models used.

177 In addition to discrete data, many landslide studies utilize time series data. When it comes to  
178 technical forecasting using time series data, machine learning regression prediction models, such as  
179 extreme learning machine (ELM) (Li et al., 2018), least squares support vector machine (LSSVM) (Liu  
180 et al., 2019), dynamic neural network (DNN) (Aggarwal et al., 2020), random forests (RFs) (Hu et al.,  
181 2021), SVM (Zhang et al., 2021), and Gaussian process regression (GPR) (Hu et al., 2019), have proven  
182 highly effective at yielding reliable results. These models also provide scalability and the ability to handle  
183 larger datasets. However, it is essential to note that machine learning models are sensitive to the white  
184 noise typical of time series features. This can pose challenges in capturing subtle behaviors and complex  
185 interrelationships, mainly when data availability is limited (Zhang et al., 2020). Finally, feature  
186 engineering (the process of selecting and transforming input variables to enhance the performance of the  
187 models) is computationally intensive and labor-intensive, limiting its applicability when rapid forecasting  
188 is required.

189 Alongside the aforementioned machine learning models, a range of neural network models, from  
190 simpler ones like Artificial Neural Networks (ANN) to more advanced approaches such as Deep Neural  
191 Networks (DNNs) and CNN, are also employed in research related to landslide (Kumar et al., 2017; Zheng  
192 et al., 2022). Notably, CNN models have become increasingly popular and are widely used in research  
193 related to this disaster. CNN models often yield superior predictive results than other models in landslide  
194 susceptibility assessment and displacement prediction (He et al., 2024).

195 Moreover, another research trend in landslide forecasting involves the use of time series deep  
196 learning models such as Recurrent Neural Networks (RNN), Long Short-Term Memory (LSTM), and

197 Gated Recurrent Units (GRUs), which use previous information to generate current outputs and provide  
198 state feedback (Yang et al., 2019; Xu et al., 2022; Yang et al., 2022; Zhang et al., 2022). These time-series  
199 deep learning models can effectively capture patterns of changes over time, making them highly suitable  
200 for time-series data in landslide-related studies. However, there has yet to be a comprehensive study that  
201 employs a combination of machine learning methods, time-series deep learning, and CNN models to  
202 compare and determine the most suitable model for predicting landslide displacement. Therefore, our  
203 research aims to address this gap.

204 Another noteworthy research trend involves using AI models to predict landslides based on spatial-  
205 temporal data. For instance, Dahal et al. (2024) utilized spatial-temporal data to pinpoint where landslides  
206 may occur and predict when they might happen and the expected landslide area density per mapping unit.  
207 The Ensemble Neural Network employed in this research yielded promising predictions, demonstrating  
208 its potential for forecasting landslides in Nepal's areas affected by the Gorkha Earthquake. However, our  
209 study only managed to gather temporal data. Consequently, the AI models developed in our research will  
210 be trained to learn and forecast time-series data.

#### 211 **2.4 Hybrid metaheuristic optimization algorithm and AI models in landslide prediction**

212 In landslide-related research, numerous studies have employed hybrid models, wherein metaheuristic  
213 optimization algorithms optimize the hyperparameters of AI models. For example, Balogun et al. (2021)  
214 studied landslide susceptibility mapping in Western Serbia. This research collected 14 different condition  
215 factors to serve as input data for the Support Vector Regression (SVR) model to predict landslide  
216 occurrences. The study results indicate that SVR models, with hyperparameters fine-tuned by optimization  
217 algorithms such as gray wolf optimization (GWO), bat algorithm (BA), and cuckoo optimization  
218 algorithm (COA), all yielded better prediction results compared to using a single model.

219 Hakim et al. (2022) conducted a study utilizing CNN models optimized by the GWO and imperialist  
220 competitive algorithm (ICA) for landslide susceptibility mapping from geo-environmental and topo-  
221 hydrological factors in Incheon, Korea. This research demonstrates that GWO and ICA effectively fine-  
222 tuned the CNN model, resulting in a highly accurate landslide susceptibility map.

223 Jaafari et al. (2022) employed an AI model known as the group method of data handling (GMDH)  
224 for classification purposes, optimizing it using the cuckoo search algorithm (CSA) and the whale  
225 optimization algorithm (WOA). In northwest Iran, they aimed to predict landslides based on various  
226 factors, including topographical, geomorphological, and other environmental factors. After training and  
227 testing, the GMDH-CSA model produced superior prediction results compared to the GMDH-WOA and  
228 the standalone GMDH model.

229 It is evident from numerous past studies on landslides that the application of metaheuristic  
230 optimization algorithms significantly enhances the predictive effectiveness of AI models. Therefore, this

231 study also incorporates this approach to ensure the model's accuracy in landslide prediction. This study  
232 will also employ a recently developed metaheuristic algorithm, including a clustering algorithm. This  
233 algorithm is promising in yielding favorable results in fine-tuning hyperparameters for AI models.

### 234 **3. Methodology**

#### 235 **3.1 Convolutional Neural Networks**

236 In 1998, LeCun introduced a novel type of DNN known as the CNN, specifically designed for  
237 processing data with a grid-like structure, such as images. The complex, layered system of CNN facilitates  
238 the automated extraction of features without extensive preprocessing, making it ideal for object  
239 recognition, image classification, and segmentation tasks. The detailed mechanism of the CNN model can  
240 be found in Appendix A.

241 This study will use various CNN models to predict deep-seated slope displacement. The CNN models  
242 employed in this research include VGG (Simonyan and Zisserman, 2014), ResNet (He et al., 2016),  
243 Inception (Szegedy et al., 2015), Xception (Chollet, 2016), MobileNet (Howard et al., 2017), DenseNet  
244 (Huang et al., 2017), and NASNet (Zoph et al., 2018). To clarify, the term "standard CNN models" will  
245 refer to models with structures that can be user-defined, while "retrained CNN models" will denote those  
246 with architectures that have been researched and developed by other scientists and have been proven to  
247 be highly effective.

248 CNN models are typically used for image processing tasks. However, the input data for this study is  
249 in numerical and vector form. Therefore, several transformation steps are required to convert this  
250 numerical and vector data into image data suitable for CNN input. Detailed information about these  
251 transformation steps can be found in the study by Chou and Nguyen 2023 (Chou and Nguyen, 2023).

#### 252 **3.2 Deep Learning Models for Time Series**

253 RNN was introduced by Elman in 1990 (Elman, 1990). This model makes predictions based on  
254 sequential data, crucial for language modeling, document classification, and time series analysis. The  
255 architecture of an RNN model can be found in Appendix B.

256 In this study, advanced models of RNN, such as LSTM [54] and GRU [55], are also utilized, and  
257 their effectiveness in predicting deep-seated landslides will be compared.

#### 258 **3.3 Machine Learning**

259 In addition to the aforementioned deep learning models, as elucidated earlier, machine learning  
260 models will be employed to predict deep-seated slope displacements in this research. The machine  
261 learning models utilized will encompass the following: linear regression (LR) (Stanton, 2001), ANN  
262 (McCulloch and Pitts, 2021), SVR (Drucker et al., 1996), classification and regression tree (CART)  
263 (Breiman, 1984), radial basis function neural network (RBFNN) (Han et al., 2010), extreme gradient

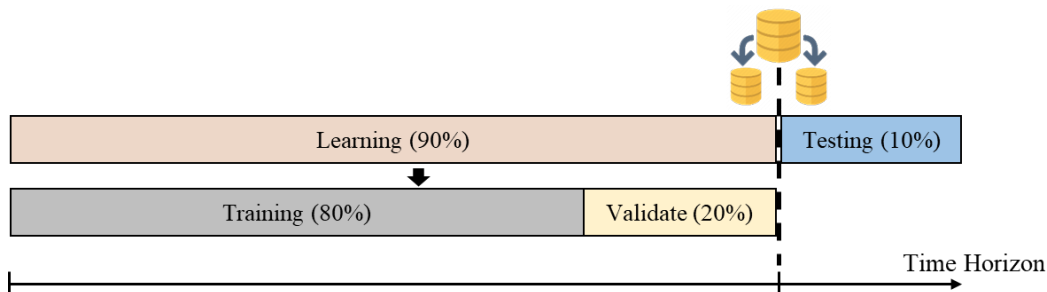


264 boosting (XGBoost) (Chen; and Guestrin). These machine learning models will be used to make  
 265 predictions and will be compared with other deep learning models.

### 266 3.4 Model Validation and Performance Metrics

#### 267 3.4.1 Evaluation and Validation

268 To obtain reliable (i.e., generalizable) evaluation and validation results, it is crucial that the data  
 269 used for testing does not include the data used for training. Therefore, a dataset must be divided into  
 270 training, validation, and testing subsets before training the AI model. Training data is used to learn patterns;  
 271 testing data is used to assess model performance and identify errors; and validation data is used to fine-  
 272 tune the hyperparameters. In the current study, we opted to refrain from employing cross-validation, which  
 273 tends to be time-consuming. Instead, we adopted the holdout approach to manage our large dataset with  
 274 well-represented target variables (Figure 2). A 90:10 ratio is generally used to split datasets into learning  
 275 and testing data (Di Nunno et al., 2023). When implementing the holdout method during hyperparameter  
 276 optimization, 20% of the learning data is used for validation, and the remaining 80% is used for training.



277  
 278 Figure 2. Data are splitting under the proposed Holdout scheme.

#### 279 3.4.2 Performance Metrics

280 This study utilized four widely recognized performance measures to assess the model's effectiveness  
 281 in prediction accuracy (Chou and Nguyen, 2023). The measures included mean absolute error (MAE),  
 282 mean absolute percentage error (MAPE), and root mean square error (RMSE).

283 MAE represents the mean of absolute errors, calculated as the average of the absolute  
 284 differences between actual and predicted values. Its advantage lies in its simplicity, which  
 285 provides a straightforward measure of average prediction error. However, a drawback of MAE is  
 286 its insensitivity to more significant errors, so it may not effectively highlight differences between  
 287 models when significant errors are present. It is defined as:

$$288 \text{MAE} = \frac{1}{n} \sum_{i=1}^n |y_i - \hat{y}_i| \quad (1)$$

289 where  $n$  is the number of predictions,  $y_i$  is the  $i^{\text{th}}$  forecasted value, and  $\hat{y}_i$  is the corresponding  $i^{\text{th}}$   
 290 actual value.

291 MAPE quantifies the average absolute error ratio to the actual value derived from the  
292 differences between actual and forecasted values. It provides a clear metric in percentage terms,  
293 facilitating straightforward interpretation across various datasets. However, MAPE's limitation  
294 arises from its sensitivity to zero values in the actual data, which can become undefined or  
295 impractical to compute, limiting its utility in scenarios involving zero or near-zero actual values.  
296 The expression for MAPE is as follows:

$$297 \quad MAPE = \frac{1}{n} \sum_{i=1}^n \left| \frac{y_i - \hat{y}_i}{y_i} \right| \quad (2)$$

298 where  $n$  is the number of predictions,  $y_i$  is the  $i^{\text{th}}$  forecasted value, and  $\hat{y}_i$  is the corresponding  $i^{\text{th}}$   
299 actual value.

300 RMSE represents the square root of the average squared error between actual and forecasted  
301 values and is widely used for its ability to indicate the dispersion of errors. This method captures  
302 the magnitude and direction of errors, making it practical for assessing overall prediction accuracy.  
303 However, RMSE tends to be more sensitive to outliers and significant errors than MAE due to its  
304 squaring of errors during computation. This sensitivity can disproportionately affect its evaluation  
305 in datasets with extreme values. The expression for RMSE is as follows:

$$306 \quad RMSE = \sqrt{\frac{1}{n} \sum_{i=1}^n (y_i - \hat{y}_i)^2} \quad (3)$$

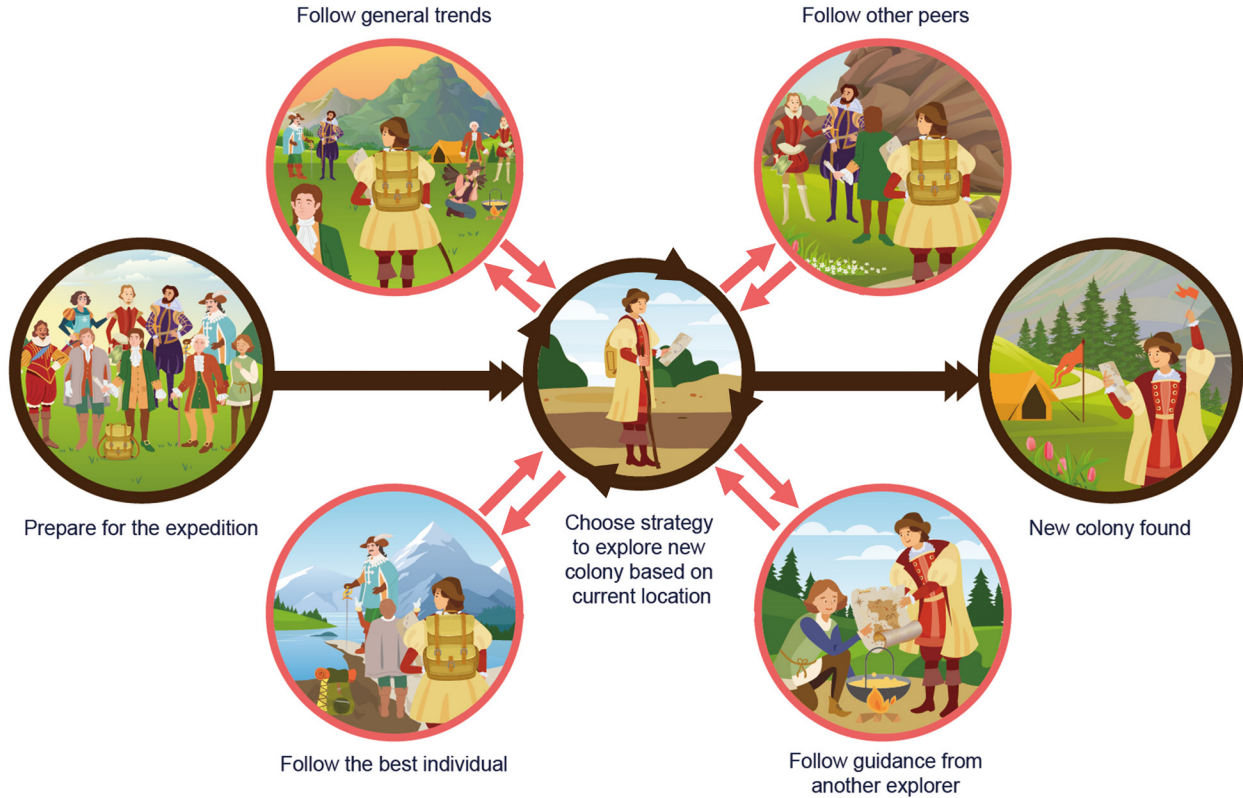
307 where  $n$  is the number of predictions,  $y_i$  is the  $i^{\text{th}}$  forecasted value, and  $\hat{y}_i$  is the corresponding  $i^{\text{th}}$   
308 actual value.

### 309 3.5 Age of Exploration-Inspired Optimizer

310 This study employs a range of AI models to forecast deep-seated displacement in mountainous  
311 regions. To enhance the prediction accuracy of these AI models, the study incorporates a novel  
312 metaheuristic optimization algorithm known as the Age of Exploration-Inspired Optimizer (AEIO).  
313 Developed by Chou and Nguyen in 2024, this algorithm has demonstrated high effectiveness in fine-  
314 tuning the hyperparameters of AI models. This algorithm treats each particle in the search domain as an  
315 explorer. The movement of particles toward regions with higher fitness values parallels the exploratory  
316 activities of the Age of Exploration, where explorers sought ideal locations for establishing colonies. In  
317 this study, each particle represents a set of hyperparameters, with the ultimate goal of the search process  
318 being to identify the optimal particle or hyperparameter set that minimizes prediction error for AI models.  
319 Figure 3 illustrates the AEIO algorithm.

320 The strength of the AEIO algorithm lies in its ability to develop specific strategies for particles based  
321 on their positions, enabling faster convergence to the optimal point. Using density-based spatial clustering

322 of applications with noise (DBSCAN) for particle clustering, the AEIO determines whether particles are  
 323 in favorable or unfavorable positions, reminiscent of explorers during the Age of Exploration. The  
 324 proximity (within clusters) allows explorers to gather information and move toward optimal locations,  
 325 thereby enhancing their ability to establish new colonies. In contrast, explorers far apart (outside clusters)  
 326 adopt different strategies, relying on limited peer guidance or general trends in their quest for new  
 327 territories.



328

329

Figure 3. Illustration of Age of Exploration-Inspired Optimizer

330

331

332

333

334

335

336

337

338

339

340

In each iteration, explorers forecast their next move. If it promises a better position, they relocate. Otherwise, if the new spot is less favorable for colony establishment, they stay put and await the next iteration. The algorithm employs specific mathematical formulas to calculate the movement step of explorers or particles in the AEIO. The exploratory steps of an explorer in the AEIO algorithm will continuously iterate until the stop condition is satisfied.

- **Explorers follow general trends**

The explorer choosing this movement type will calculate the distance from their location  $x_{i,d}(t)$  to the center of all other explorers ( $Meanvl_d(t)$ ), then attempt to move towards that central point in the hope of finding a better location with the potential to establish a new colony. The following formula determines the explorer's position after the movement:

$$x_{i,d}(t + 1) = x_{i,d}(t) + \alpha * (Meanvl_d(t) - x_{i,d}(t)) \times rand(0,1) \times R \quad (4)$$

$$341 \quad Meanvl_d(t) = \frac{x_{1,d}(t)+x_{2,d}(t)+\dots+x_{n_{Pop},d}(t)}{n_{Pop}} \quad (5)$$

342 where  $d = 1,2, \dots D$ ;  $D$  is the number of dimensions;  $i = 1,2, \dots n_{Pop}$ ;  $n_{Pop}$  is the total number of  
 343 explorers;  $t = 1,2, \dots MaxIt$  is the number of iterations;  $MaxIt$  is the maximum value of iteration;  $\alpha$  is a  
 344 parameter for adjusting the particle's movement toward the centroid position (usually equals 3).  
 345  $Meanvl_d(t)$  is the centroid of all particles in dimension  $d$ .  $rand(0,1)$  is the random number in the range  
 346  $[0,1]$ .  $R$ : a number that equals 1 or 2 depending on the value of  $rand(0, 1)$  per the equation.  $R =$   
 347  $round(1 + rand(0,1) \times 1)$ ,  $x_{i,d}(t)$  is the location of particle  $i$  in iteration  $t$ ,  $x_{i,d}(t + 1)$  is the location  
 348 of particle  $i$  in iteration  $(t + 1)$ .

349 • **Explorers follow three other peers**

350 Explorers employing this movement method will calculate the average position of three randomly  
 351 selected other explorers  $\left(\frac{x_{1,d}(t)+x_{2,d}(t)+x_{3,d}(t)}{3}\right)$  and then move toward this newly calculated average  
 352 position. The explorer's new position is computed using the following formula:

$$353 \quad x_{i,d}(t + 1) = x_{i,d}(t) + \left(\frac{x_{1,d}(t)+x_{2,d}(t)+x_{3,d}(t)}{3} - x_{i,d}(t)\right) \times rand(0,1) \times R \quad (6)$$

354 where:  $x_{1,d}(t)$ ,  $x_{2,d}(t)$  and  $x_{3,d}(t)$  are three random explorers in dimension  $d$  at iteration  $t$ ,  $d = 1,2, \dots D$ ;  
 355  $D$  is the number of dimensions;  $i = 1,2, \dots n_{Pop}$ ;  $n_{Pop}$  is the total number of explorers;  $t = 1,2, \dots MaxIt$   
 356 is the number of iterations;  $MaxIt$  is the maximum value of iteration.

357 • **Explorers follow the best one**

358 According to this strategy, the explorer ( $x_{i,d}(t)$ ) will move closer to the position of another explorer  
 359 currently holding the best position ( $Best_d(t)$ ), as determined by the following formula:

$$360 \quad x_{i,d}(t + 1) = x_{i,d}(t) + (Best_d(t) - x_{i,d}(t)) \times rand(0,1) \times R \quad (7)$$

361 where:  $Best_d(t)$  represents the position of the particle with the best fitness in dimension  $d$  at iteration  $t$ ,  
 362 the parameters  $d$  and  $t$  hold the same significance as defined in Equation 10.

363 • **Explorers follow guidance from another one**

364 Explorers in favorable positions with access to information can execute this movement strategy. In  
 365 this scenario, explorers ( $x_{i,d}(t)$ ) will consult with ~~each other~~ another explorer. The consulted explorer will  
 366 compare their direction and distance to the best individual, who holds the most favorable position  
 367 ( $Best_d(t)$ ) and guide the inquirer. This algorithm assumes that the inquirer can be any explorer, i.e., a  
 368 random explorer ( $x_{1,d}(t)$ ). The following formula describes how to calculate the new position of the  
 369 explorer following this strategy:

$$370 \quad x_{i,d}(t + 1) = x_{i,d}(t) + (Best_d(t) - x_{1,d}(t)) \times rand(0,1) \times R \quad (8)$$

371 where:  $x_{1,d}(t)$  is a random explorer in dimension  $d$  at iteration  $t$ . the parameters  $d$  and  $t$  hold the same  
 372 significance as defined in Equation 10.

373 • **Crowd control mechanism**

374 To enhance the efficiency of AEIO in transitioning between exploration and exploitation, a  
375 mechanism is employed to adjust the parameters of DBSCAN throughout each cycle, according to the  
376 following formula:

377 
$$\varepsilon_d = \left(0.1 + \frac{t}{MaxIt}\right) \times (Meanvl_d(t) - Best_d(t)) \quad (9)$$

378 
$$MinPts = round\left(1 + \frac{t}{MaxIt} \times 10\right) \quad (10)$$

379 The exploratory steps in the AEIO algorithm begin by classifying positions using the DBSCAN  
380 algorithm. Subsequently, the explorers update the crowd control mechanism according to equations (13)  
381 and (14), and move according to various strategies defined by equations (8), (10), (11), and (12). This  
382 process is conducted iteratively until the maximum number of iterations is reached.

383 To fine-tune the hyperparameters of AI models, the AEIO algorithm treats each hyperparameter as  
384 a variable. Furthermore, the objective function of the AEIO algorithm seeks to minimize the prediction  
385 error of AI models, which is quantified by an evaluation metric (MAPE). Figure 4 presents a flowchart  
386 illustrating the process by which the AEIO algorithm aids in fine-tuning hyperparameters for AI models.

387 **3.6 Experiment Setup**

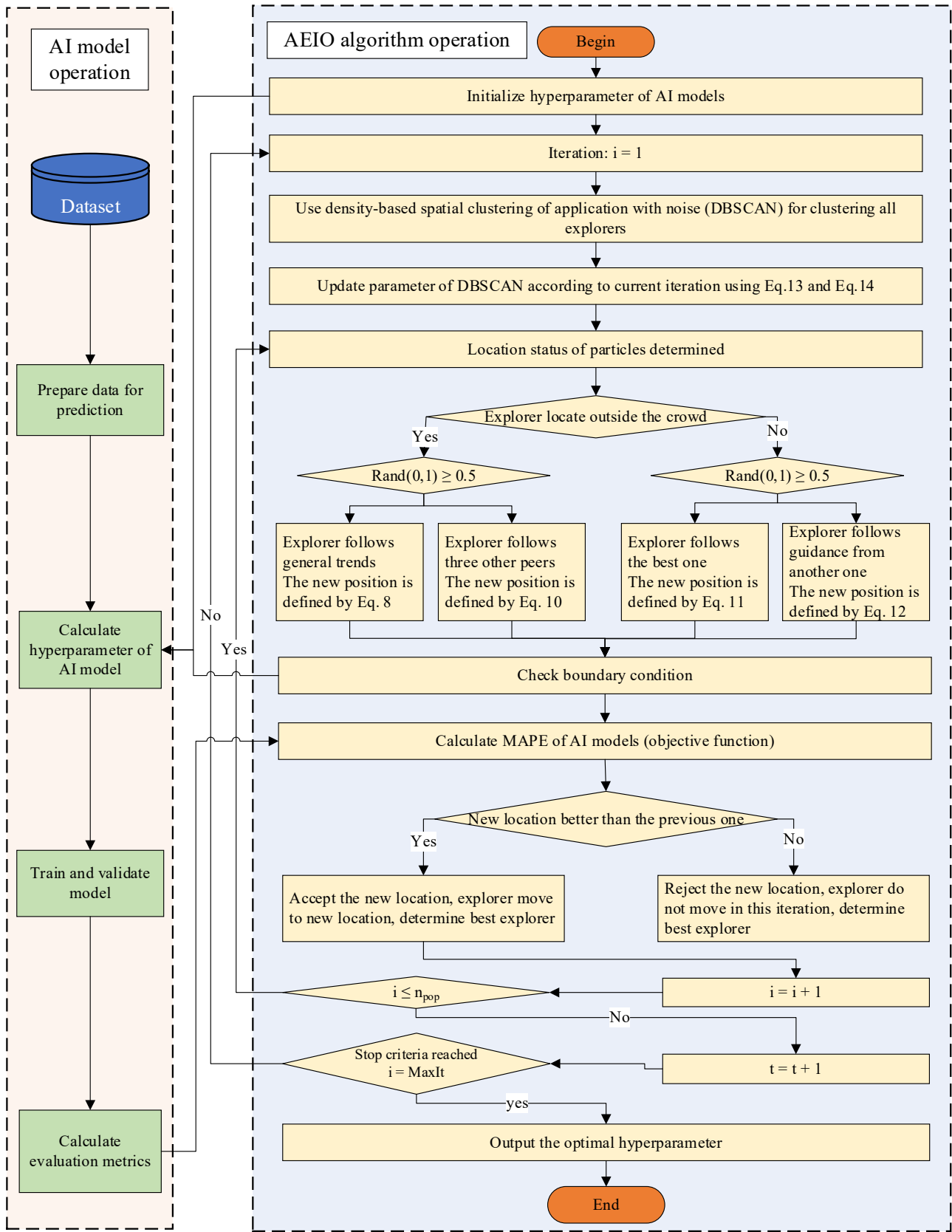
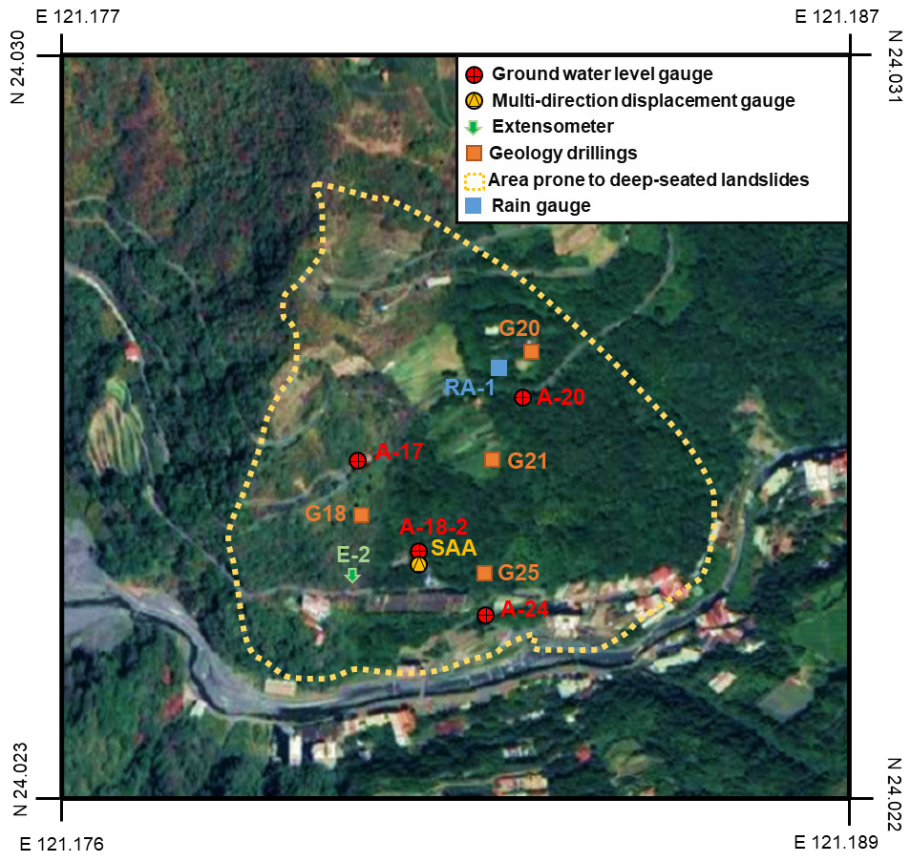


Figure 4. Flowchart of the fine-tuning process of AI models by the AEIO algorithm

3.6.1 Research Area

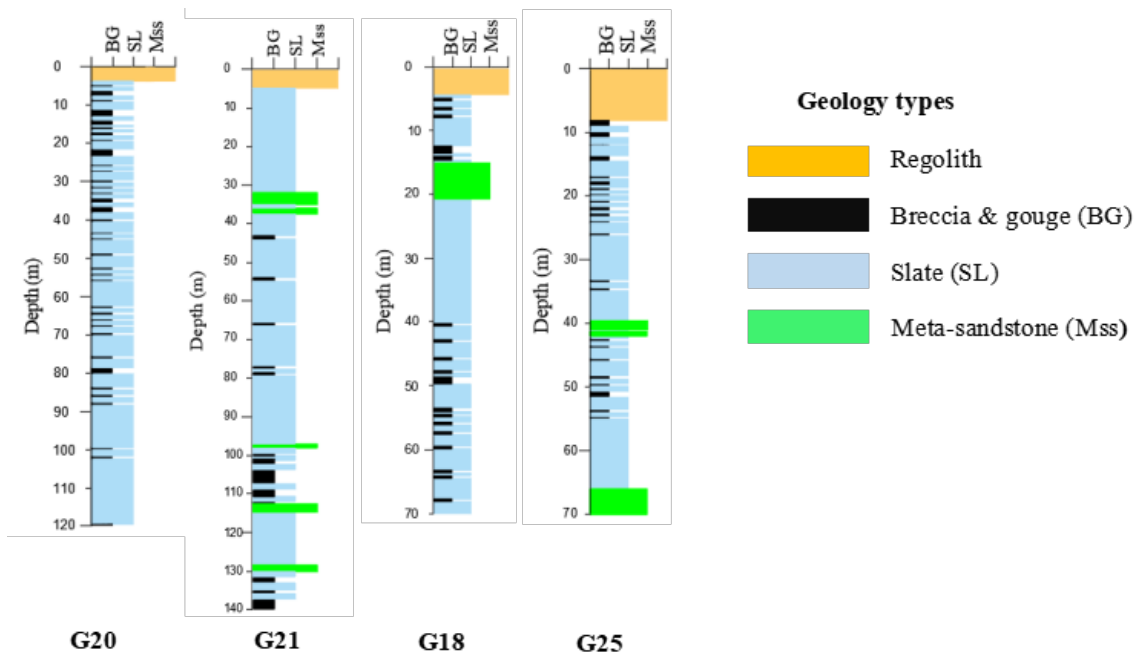
388  
389  
390  
391



392  
393  
394

Image source: Imagery ©2022 CNES/Airbus, Maxar Technologies, Map data ©2022 Google

Figure 5. Locations of measurement devices



395  
396

Figure 6. Illustration of geological drilling survey

397 The current study focuses on the northern slope of Lushan hot spring in Ren'ai Township, Nantou  
398 County (Figure 5), with Nenggao Mountain to the east, Hehuan Peaks to the north, Zhuoshe Mountain to  
399 the south, and Puli Basins to the west. The terrain features rugged mountain ranges, youthful valleys, and

400 notable river erosion (Lee and Chi, 2011). Lushan Hot Springs is located below the hill, and the main  
401 access roads for nearby settlements and hot spring sites include Provincial Highway 14 and County  
402 Highway 87.

403 In an early study of deep landslides in this area, Lin et al. (2020) reported that the Lushan slope  
404 exhibits large-scale deep-seated gravitational slope deformation, characterized by a steep scarp, a gently  
405 inclined head, and a curving river at its base. Figure 6 illustrates the geological details of the research area  
406 and shows the distribution of four survey boreholes (G20, G21, G18, and G25) along the slope. Regolith,  
407 slate, and meta-sandstone are three distinct lithological units revealed through drilling. Additionally, the  
408 study by Lin et al. identified the depths of failure planes in these survey boreholes. Specifically, boreholes  
409 G18 and G25 did not record any failure planes, while boreholes G20 and G21 recorded failure planes at  
410 depths of 85 meters and 106 meters, respectively. These failure planes were identified based on  
411 inclinometer data from the corresponding study (Lin et al., 2020).

412 Initially, the thickness of the topmost regolith layer was found to be less than 10 meters. Secondly,  
413 slate predominated, exhibiting a notable presence with sporadic evidence of weathering that resulted in  
414 brecciated patterns. This composition frequently broke into breccia and gouges, particularly along  
415 cleavage planes and thin shear zones, indicating its susceptibility to collapse. This geological layer is  
416 identified as the area's primary cause of landslide risk. Finally, meta-sandstone appeared intermittent  
417 compared to the more prevalent lithological units, characterized by its fragility and fractures and occurring  
418 less frequently in the drilled samples.

419 Previous research has detected signs of brittle deformation in the area. These indications include  
420 chevron folds within cleavages, visible cracks, and intricate jigsaw puzzle-like patterns at the head of the  
421 rock formations. Overturned and flexural toppling cleavages are prevalent towards the toe of the slope.  
422 Additionally, kink bands are observable on fractures recently undergoing flexural folding along the eastern  
423 boundary. Notably, horizontal cleavages near the toe region also exhibit inter-cleavage gouges. Further  
424 details on this geological information can be found in the study by Lin et al. (2020). These instances  
425 highlight the potential for significant geological changes and landslide risk in this region.

### 426 **3.6.2 Data Collection and Preprocessing**

427 In this study, hourly data of deep-seated displacement and groundwater level were collected by the  
428 Department of Civil Engineering, College of Science and Technology, at the National Chi Nan University  
429 research group over eight years from July 2009 to June 2017, yielding 68,317 data points. The installation  
430 time points and locations are presented in Table 1 and Figure 5, respectively.

431 The data used in this study were collected using an in-hole telescopic gauge (E-2), a multidirectional  
432 shape acceleration array sensor (SAA) with an underground displacement gauge, and four groundwater



433 level gauges (A-17, A-18-2, A-20, and A-24). The transmission, storage, and processing of data are  
 434 described in detail in the research of Lau et al. (2023).

435 The operation of the in-hole extensometer entailed the installation of a borehole through the sliding  
 436 surface. One end of a steel cable was anchored at the bottom, and a displacement gauge was placed at the  
 437 free end to measure deformations automatically. The fixed stops for E-2 and SAA were situated at depths  
 438 of 70 meters and 40 meters below the surface, respectively. In addition to groundwater level data,  
 439 information regarding significant rainfall events in this area was also measured and is presented in Table  
 440 2.

441 Table 1. Device installation timepoints

Year	2008	2009	2010	2011	2012	2013	2014	2015	2016	2017
<b>Groundwater level gauge</b>	A-17									
	No data						A-18-2			
	No data	A-20								
	No data	A-24								
<b>Extensometer</b>	No data	E-2								
	No data			SAA						

442

443 Table 2. Heavy rainfall events in the study area

No.	Rain onset (month/day/year hour: minute)	Rain end time (month/day/year hour: minute)	Accumulating rainfall (mm)	Drop rain hour (hr)	Event
1	7/17/2008 14:00	7/19/2008 21:00	418	55	Kameiji typhoon
2	9/11/2008 16:00	9/15/2008 12:00	943.5	92	Pungentmusc typhoon
3	9/28/2008 1:00	9/30/2008 10:00	523.5	57	Rose honey typhoon
4	8/4/2009 3:00	8/12/2009 20:00	931	209	Mopull typhoon
5	6/8/2012 13:00	6/17/2012 16:00	1029	219	Torrential rain
6	7/30/2012 7:00	8/3/2012 11:00	370	100	Supull typhoon
7	5/10/2013 16:00	5/25/2013 1:00	597	345	Torrential rain
8	7/12/2013 19:00	7/15/2013 23:00	330	76	Suprofit typhoon
9	9/20/2013 22:00	9/23/2013 18:00	347	68	Usagi typhoon
10	5/9/2014 5:00	5/22/2014 3:00	326.5	310	Torrential rain
11	7/22/2014 14:00	7/24/2014 0:00	321.5	34	Madham typhoon
12	6/1/2017 11:00	6/4/2017 21:00	897	82	Torrential rain
13	6/11/2017 17:00	6/19/2017 3:00	638.5	178	Torrential rain

444 Based on the collected data, analyses have examined the correlation between groundwater levels  
 445 and deep-seated displacement at Lushan Mountain. To observe this correlation, graphs illustrating the

446 precipitation of recorded heavy rainfall (Figure 7A), variations in displacement (Figure 7B and Figure  
447 7C), and groundwater levels (Figure 7D) over time have been plotted.

448

449

450

451  
452

453  
454

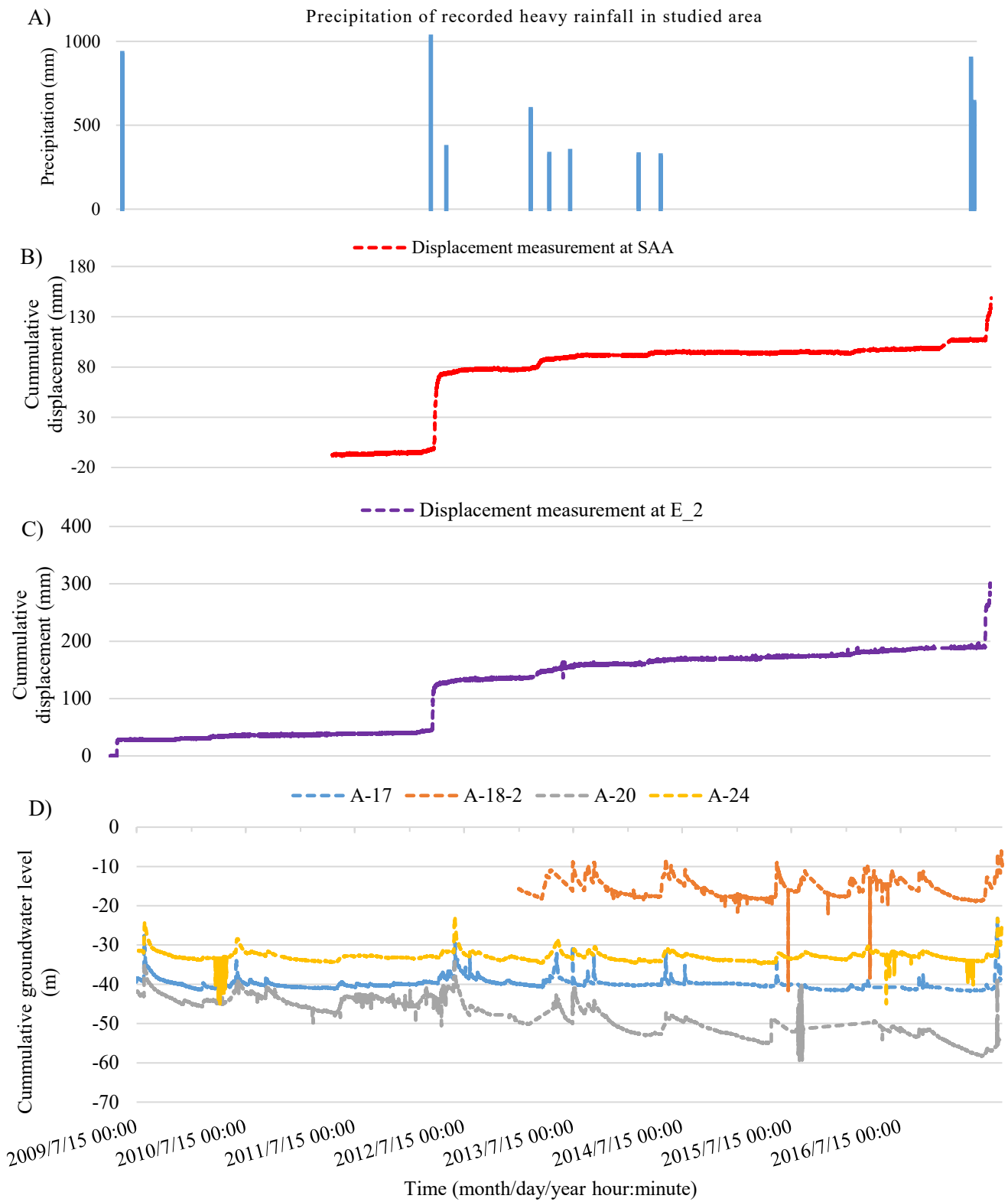


Figure 7. Unified timeline visualization of data in this study.

A) Precipitation of recorded heavy rainfall in the studied area; B) Measured displacements from extensometer SAA C) Measured displacements from extensometer E\_2; D) Groundwater levels at stations A-17, A-18-2, A-20, and A-24.

455 The graphs above show that the displacement values at both stations often exhibit significant  
456 increases coinciding with periods of pronounced fluctuations in groundwater levels. Specifically, in June  
457 2012, there was a notable surge in groundwater levels attributed to heavy rainfall from June 8, 2012, to  
458 June 17, 2012, totaling 1029 mm over 219 hours (as indicated in Table 2 and Figure 7A). The abnormal  
459 rise in groundwater levels caused a structural alteration in the area's soil, consequently amplifying deep-  
460 seated displacement at both stations, namely E\_2 and SAA, as evidenced in Figure 7B and Figure 7C.

461 Similar events occurred in November 2017. Heavy rainfall totaling 638.5 mm over 178 hours during  
462 this period also caused a sudden alteration in groundwater levels, resulting in significant deep-seated  
463 displacement. Through comparison, it is apparent that there were up to 13 instances of anomalous heavy  
464 rainfall during the study period. However, not every example of heavy rain resulted in significant  
465 fluctuations in groundwater levels, leading to substantial displacement. Hence, data regarding  
466 groundwater level elevation will be used to predict deep-seated landslides rather than rainfall data.

467 In addition to groundwater level data, weather factors such as temperature and humidity are also  
468 utilized as input data for the prediction model. This study includes temperature as an input variable for AI  
469 models to predict deep-seated displacement due to its impact on soil structure. Elevated temperatures can  
470 cause thermal expansion of soil particles, which can increase pore water pressure and reduce effective  
471 frictional resistance forces (Pinyol et al., 2018). Additionally, previous research has shown a relationship  
472 between temperature and the likelihood of landslides in clay-rich soils, which are also present in the  
473 geological composition of Lushan Mountain (Shibasaki et al., 2017; Loche and Scaringi, 2023).

474 This study collected groundwater level and displacement data on-site using sensors. Furthermore,  
475 temperature and humidity data were obtained from the website <https://power.larc.nasa.gov>. This dataset  
476 is part of the Prediction of Worldwide Energy Resource (POWER) project, developed by the National  
477 Aeronautics and Space Administration (NASA) of the United States. The POWER solar data derives from  
478 satellite observations, which are used to infer surface insolation values. Meteorological parameters are  
479 sourced from the Modern-Era Retrospective analysis for Research and Applications, Version 2 (MERRA-  
480 2) assimilation model. The primary solar data is available with a global resolution of  $1^\circ \times 1^\circ$   
481 latitude/longitude, while the meteorological data is provided at a finer resolution of  $\frac{1}{2}^\circ \times \frac{5}{8}^\circ$   
482 latitude/longitude. Users can download the data hourly, daily, or monthly through this website.

483 Table 3 displays the input and output variables for AI models to predict deep-seated displacement at  
484 Lushan Mountain. Two datasets will be generated: one for predicting displacement at the E\_2 station and  
485 another for indicating displacement at the SAA station. Table 4 outlines the number of data points for each  
486 dataset and illustrates how the data is divided into training and testing sets.

487 Table 3. Input and output variables of a model predicting deep-seated displacement.

	Attributes group	Attributes	Variable ID	Dataset of E_2 station	Dataset of SAA station
Output variables	Deep-seated displacement measures	Displacement extensometer at station E_2 (mm)	Y1	✓	-
		Displacement extensometer at station SAA (mm)	Y2	-	✓
Input variables	Groundwater level data	Groundwater level at station A-17 (m)	X1	✓	✓
		Groundwater level at station A-18-2 (m)	X2	✓	✓
		Groundwater level at station A-20 (m)	X3	✓	✓
		Groundwater level at station A-24 (m)	X4	✓	✓
	Weather data	Temperature at 2 meters (°C)	X5	✓	✓
		Specific humidity at 2 meters (g/kg)	X6	✓	✓

488 Table 4. Number of data points

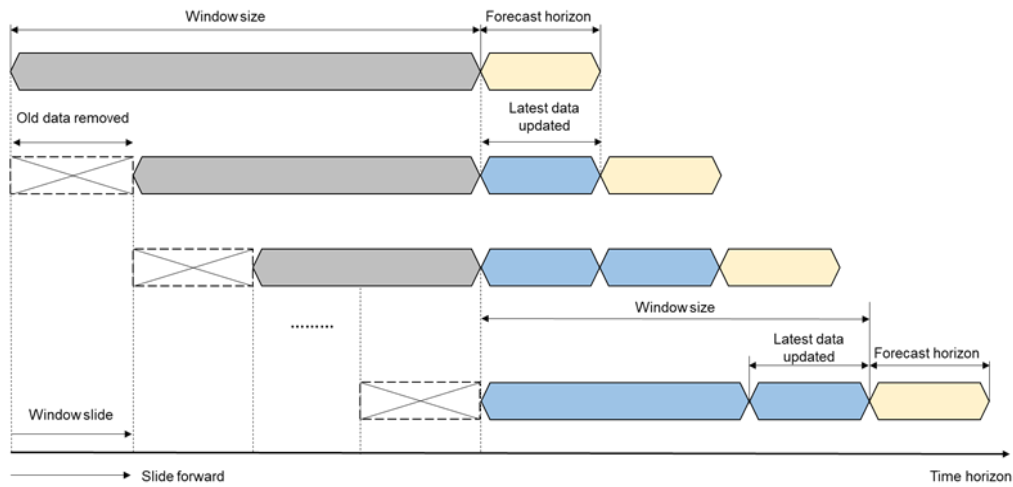
Quantity of data points	Dataset of the E-2 station	Dataset of SAA station
Total data samples	68312	51679
Count of training samples (90% of the total sample)	61477 (2009/07/15-2016/09/07)	46523 (2011/07/13 – 2016/11/16)
Count of testing samples (10% of the total sample)	6835 (2016/09/07-2017/06/20)	5156 (2016/11/16-2017/06/20)

489 **3.6.3 Data Preprocessing**

490 Firstly, the data in this study will undergo a normalization process to scale all features to a consistent  
 491 range (typically between 0 and 1). This step is essential to ensure that the model considers the importance  
 492 of each feature, thereby enhancing overall prediction accuracy (Han et al., 2006).

493 In the current study, the sliding window technique is implemented after data normalization to  
 494 organize data according to a specific time frame. This involves using historical data from previous steps  
 495 to predict the output for subsequent steps (Chou and Ngo, 2016). The forecasting horizon refers to the  
 496 length of time into the future for which output forecasts are made.

497 The basic process of the sliding window technique is illustrated in Figure 8. To train AI models, this  
 498 study opts for a window size of one week (equivalent to 168 hours). This fixed window size is utilized  
 499 exclusively for single AI models. Subsequently, the hybrid model's AEIO algorithm and other  
 500 hyperparameters will fine-tune the window size to determine the most suitable settings.



501  
 502 Figure 8. Sliding window technique

503 This study focuses on predicting deep displacement values at two distinct time intervals: 1 day ahead  
 504 (+24 hours) and seven days ahead (+168 hours). These forecast horizons are strategically chosen to  
 505 provide timely information, enabling management departments to make accurate decisions regarding  
 506 evacuating people and assets from areas prone to landslides.

507 Specifically, for valuable assets and machinery that require time for relocation from landslide-prone  
 508 areas, having advance knowledge of the landslide event one week ahead of relocation is crucial.  
 509 Furthermore, for humans, animals, or other assets that can be evacuated more swiftly, predicting the  
 510 landslide one day in advance is sufficient to ensure safety.

511 The predicted outputs are quantified in mm/day, facilitating decision-making for administrators  
 512 according to the TGS-SLOPEM106 standard (Ruitang et al., 2017). Table 5 outlines suggested actions  
 513 corresponding to different degrees of deep displacement as per the TGS-SLOPEM106 standard issued by  
 514 the Taiwan government.

515 Table 5. Recommendations are taken from TGS-SLOPEM106 for addressing displacement values in the  
 516 early stages of deep sliding.

Classification of the displacement value	Attention value	Warning value	Action value
Corresponding displacement value	2 mm/month	0.5 mm/day	10 mm/day

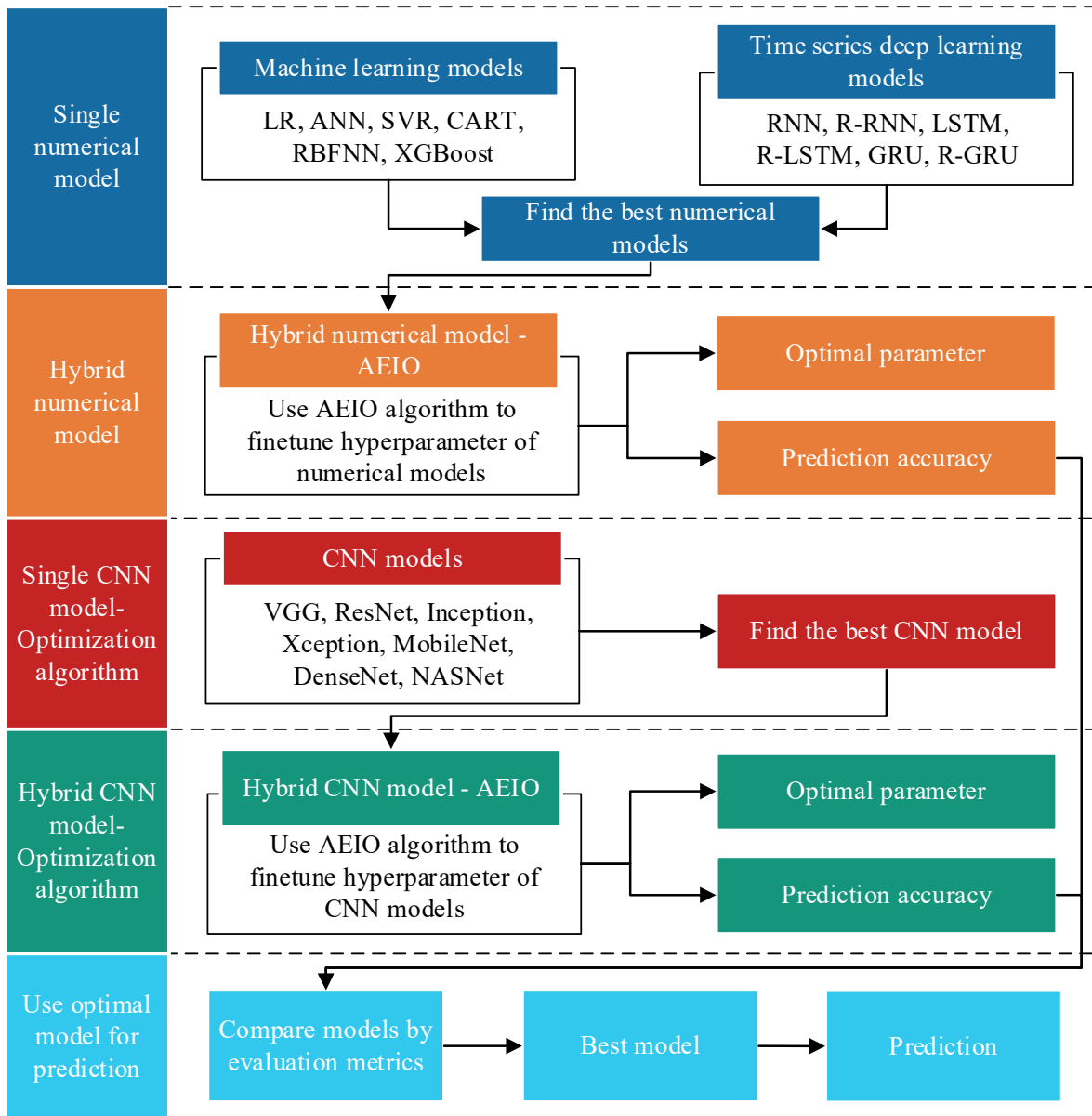
<b>Classification of the displacement value</b>	<b>Attention value</b>	<b>Warning value</b>	<b>Action value</b>
Condition of slopes	The slope started to slip or slowly move	The hill is undergoing constant-velocity descent.	The rate of slope movement is increasing, elevating the risk of collapse.
Recommendations on monitoring activities	- Inspect the monitoring system for any irregularities and consider increasing the frequency of visual inspections	- Enhance the frequency of the automated monitoring system	- Implement a rigorous monitoring system frequency
Countermeasures	- Conduct a slope stability investigation and assessment - Develop a reinforcement and improvement plan to enhance slope stability	- Execute emergency slope reinforcement procedures - Develop an emergency response plan for individuals and vehicles within the landslide area	- Evacuate people and vehicles from the landslide area

517 **4. Model Establishment and Analysis Results**

518 **4.1 Model Establishment**

519 Predicting deep-seated displacement at Lushan Mountain is undoubtedly highly challenging, given  
520 that such landslides depend on numerous factors. Therefore, multiple methods will be employed  
521 simultaneously to identify the optimal AI model for prediction. These methods include single machine  
522 learning, time series deep learning, CNN, and hybrid models.

523 This study will conduct a testing process to systematically identify the optimal model capable of  
524 accurately predicting deep-seated landslides. An illustration of this process can be found in Figure 9.  
525 Initially, the study will sequentially employ various single numerical AI models, such as machine learning  
526 models (LR, ANN, SVR, CART, RBFNN, XGBoost) and time series deep learning models (RNN, R-  
527 RNN, LSTM, R-LSTM, GRU, R-GRU), to forecast displacement.



528

529 Figure 9. Diagram depicting the steps of choosing the optimal AI model to predict deep-seated  
 530 displacement

531 Subsequently, the model with the highest prediction accuracy will be selected for integration with  
 532 the AEIO algorithm, forming a hybrid model. In this hybrid model, the hyperparameters of the best  
 533 numerical AI model will be fine-tuned by the AEIO algorithm to enhance prediction accuracy.

534 In addition to the numerical AI models, this study employs individual CNN models for predicting  
 535 deep-seated displacement. Subsequently, similar to the approach above, the best CNN model with the  
 536 highest displacement prediction capability will be fine-tuned by the AEIO algorithm within a hybrid  
 537 model. In the final step, a comparison process between the two hybrid models— one comprising the best  
 538 numerical model and the other involving the best CNN model fine-tuned by AEIO— will be conducted  
 539 to select the optimal model for this study.

540 **4.2 Analysis Results**

541 This section will present the experimental results of the steps outlined in Figure 9, along with relevant  
 542 metrics and analysis.

#### 543 4.2.1 AI Models

##### 544 a. Machine Learning Models

545 Initially, single machine learning models will be employed to predict deep-seated displacement. In  
 546 this phase, machine learning models will utilize default hyperparameters, as detailed in the research of  
 547 Chou and Nguyen (2023). The prediction results of these models at both E-2 and SAA stations are  
 548 displayed in Table 6. These results show that most machine learning models demonstrate a relatively good  
 549 predictive capability for displacement, particularly the XGBoost model, which exhibits MAPE values  
 550 ranging from 8.14% to 9.58%. Following closely, CART also produces favorable prediction results, with  
 551 MAPE ranging from 8.53% to 9.76%. Regarding prediction accuracy, XGBoost and CART models  
 552 outperform LR, ANN, SVR, and RBFNN models.

553 Table 6. Performance results of machine learning models for predicting deep-seated displacement.

Model	MAPE (%)		MAE (mm)		RMSE (mm)		Time (s)	
	1-day-ahead	7-day-ahead	1-day-ahead	7-day-ahead	1-day-ahead	7-day-ahead	1-day-ahead	7-day-ahead
<b>E-2-station</b>								
LR	10.70	11.22	22.61	21.32	28.17	31.96	0.0001	0.003
ANN	12.31	13.31	22.19	24.92	26.56	32.54	129.80	212.83
SVR	12.46	12.47	21.98	22.56	26.27	28.05	162.55	174.44
CART	8.53	8.67	15.67	16.87	25.16	27.81	1.50	2.57
RBFNN	15.13	15.19	23.81	22.56	28.42	31.96	2.32	4.10
XGBoost	<b>8.14</b>	<b>8.36</b>	14.80	14.68	23.07	23.92	1.58	3.28
<b>SAA-station</b>								
LR	11.18	12.11	11.51	11.64	17.26	16.07	0.01	0.01
ANN	10.91	10.93	9.43	10.45	16.55	15.92	116.78	190.69
SVR	10.55	10.94	10.87	9.18	15.64	13.42	136.01	346.30
CART	10.57	10.76	7.11	7.30	13.51	10.63	0.91	1.59
RBFNN	14.51	14.95	11.38	12.68	17.13	19.06	4.20	8.76
XGBoost	<b>9.17</b>	<b>9.58</b>	8.43	7.83	16.36	16.97	1.12	2.29

554 Moreover, the results in Table 6 also indicate that there is not a significant difference in the prediction  
 555 errors of the machine learning models at both E-2 and SAA stations, as the error values for both stations  
 556 are nearly equal across all machine learning models. Regarding the running time, the LR model  
 557 demonstrates the shortest duration, ranging from 0.001 to 0.1 seconds for all runs. However, the prediction



558 accuracy of this model could be higher, as mentioned earlier. In this case, the machine learning model  
 559 with the longest running time is SVR, ranging from 136.01 to 346.3 seconds. This, combined with the low  
 560 MAPE score, indicates that the SVR model operates inefficiently with the dataset in this study. After  
 561 reviewing the results of the machine learning models in this section, it is observed that XGBoost is the  
 562 most suitable machine learning model for predicting deep-seated landslides, exhibiting both high  
 563 prediction accuracy and a short running time.

#### 564 **b. Time series deep learning models**

565 Similar to the machine learning models, in this section, the time series deep learning models will  
 566 also be trained with default hyperparameters, as found in the research of Chou and Nguyen (2023). The  
 567 performance results of these models are shown in Table 7. Overall, akin to the machine learning models,  
 568 the time series deep learning models also demonstrate fairly good prediction accuracy, especially the best  
 569 model - R-GRU model, with MAPE ranging from 7.95 to 9.13%.

570 The performance of the R-GRU model surpasses that of the GRU model because the R-GRU model  
 571 learns patterns from time series data in both forward and backward directions on the timeline, thereby  
 572 capturing more patterns. Furthermore, the R-GRU model produces significantly better prediction results  
 573 with a more complex learning mechanism than other time series deep learning models. However, due to  
 574 its complex operational mechanism, the R-GRU model also requires more processing time than other time  
 575 series deep learning models. From the results of Table 7, it is observed that the operating time of the R-  
 576 GRU model ranges from 79.81 to 212.75 seconds.

577 From the conducted analyses, R-GRU has been identified as the best time series deep learning model,  
 578 owing to its excellent prediction performance. Compared to the best machine learning model, XGBoost  
 579 (with MAPE ranging from 8.14% to 9.58%), the R-GRU model (with MAPE ranging from 7.90 to 9.13%)  
 580 demonstrates higher prediction accuracy. Therefore, the R-GRU model will be chosen as the best  
 581 numerical AI model.

582 Table 7. Performance results of time series deep learning models for predicting deep-seated displacement

Model	MAPE (%)		MAE (mm)		RMSE (mm)		Time (s)	
	1-day-ahead	7-day-ahead	1-day-ahead	7-day-ahead	1-day-ahead	7-day-ahead	1-day-ahead	7-day-ahead
<b>E-2-station</b>								
RNN	12.72	12.92	23.61	24.75	31.18	29.62	83.24	177.53
R-RNN	12.31	12.84	22.88	21.97	30.20	34.42	91.47	114.33
LSTM	8.42	8.57	17.87	16.31	21.41	22.98	123.10	151.91
R-LSTM	8.13	8.75	16.63	17.84	22.85	24.67	148.56	161.14
GRU	8.43	10.15	16.06	19.38	22.46	26.75	141.50	164.26

Model	MAPE (%)		MAE (mm)		RMSE (mm)		Time (s)	
	1-day-ahead	7-day-ahead	1-day-ahead	7-day-ahead	1-day-ahead	7-day-ahead	1-day-ahead	7-day-ahead
R-GRU	<b>7.90</b>	<b>8.16</b>	15.09	15.69	20.84	23.32	156.97	172.96
<b>SAA-station</b>								
RNN	11.92	13.98	17.61	12.65	25.71	23.19	36.77	60.31
R-RNN	14.60	14.73	18.77	13.85	26.19	24.97	49.26	59.06
LSTM	10.64	10.94	12.73	12.25	29.21	29.57	62.84	113.76
R-LSTM	10.14	10.35	11.77	11.60	26.10	27.48	70.94	87.48
GRU	9.32	9.28	18.05	18.11	25.26	22.41	69.56	211.77
R-GRU	<b>8.03</b>	<b>9.13</b>	18.84	17.85	21.57	21.86	79.81	212.75

#### 583 4.2.2 Best AI Model Finetuned by AEIO Algorithm

584 This section will focus on fine-tuning the hyperparameters of the numerical model to enhance its  
585 performance in predicting deep-seated displacement. The AEIO algorithm will fine-tune the  
586 hyperparameters of the study's best numerical AI model, the R-GRU model. Details regarding the names  
587 and search ranges of the hyperparameters are outlined in Table 8. The objective function of the AEIO  
588 algorithm during the fine-tuning process is to minimize the MAPE value of the R-GRU model.

589 Table 9 illustrates the results of the fine-tuning process. From this table, it is observed that the AEIO  
590 algorithm has successfully identified the optimal hyperparameters of the R-GRU model, significantly  
591 improving the prediction accuracy of this model. For instance, the MAPE in predicting 1-day-ahead  
592 displacement of R-GRU before fine-tuning was 7.9%, but this number decreased to only 3.03% after fine-  
593 tuning.

594 Fine-tuning the R-GRU model using AEIO will maximize its potential, minimizing the prediction  
595 error to the lowest possible level. Therefore, the results obtained in this section reflect the actual quality  
596 of the dataset as well as the level of difficulty in prediction. Specifically, based on the results in Table 9,  
597 it is observed that the predictions for one-day ahead displacement (with MAPE of 3.03% and 3.94%)  
598 consistently outperform those for seven-days ahead displacement (with MAPE of 6.38% and 7.96%).

599 One-day-ahead predictions have a shorter time horizon, making them less affected by environmental  
600 fluctuations and making changes more accessible to predict. Conversely, in the case of seven-day-ahead  
601 displacement prediction, this timeframe is long enough for various factors, such as weather conditions and  
602 human interventions, to occur, increasing uncertainty and volatility in the predicted figures.

603 Additionally, Table 9 indicates that predictions from the dataset of the E-2 station consistently  
604 outperform those of the SAA station. Specifically, the displacement prediction at the E-2 station is 3.03%  
605 and 6.38%, better than the corresponding numbers for the SAA station, which are 3.94% and 7.96%,

606 respectively. This is attributed to the dataset collected by the E-2 station being more comprehensive and  
 607 gathered over a more extended period than the SAA station (as shown in Table 4).

608 Table 10 presents the optimal hyperparameters identified by the AEIO algorithm. Furthermore, in  
 609 terms of running time, most models, after fine-tuning, exhibit longer running times compared to the  
 610 original model. However, this increase is entirely acceptable since the additional running time is minimal,  
 611 and the benefits of fine-tuning are significant, as mentioned above, aiding in the model's more efficient  
 612 operation.

613 Table 8. Search ranges of the hyperparameters of the optimal hybrid numerical models (Chou and Nguyen,  
 614 2023).

Hybrid model	Hyperparameter	Search range
AEIO-R-GRU	Window size	[1-720]
	Number of hidden units	[1-400]
	Learning rate	[0.0001, 0.5]
	Dropout	[0.00, 0.99]
	Number of epochs	[10, 120]
	Batch size	[32, 64]

615 Table 9. Performance results of hybrid time-series deep learning model with AEIO in deep-seated  
 616 landslide prediction

	Model	MAPE (%)	MAE (mm)	RMSE (mm)	Time (s)
<b>One-day-ahead displacement prediction</b>	<b>E-2-station</b>				
	AEIO-R-GRU	3.03	6.89	17.98	196
	<b>SAA-station</b>				
	AEIO-R-GRU	3.94	4.16	11.20	184
<b>Seven-day-ahead of displacement prediction</b>	<b>E-2-station</b>				
	AEIO-R-GRU	6.38	10.02	18.05	261
	<b>SAA-station</b>				
	AEIO-R-GRU	7.96	12.49	7.82	248

617  
 618 Table 10. Optimal hyperparameter of time series deep learning model found by AEIO algorithm

Model	Window size	Number of hidden units	Dropout rate	Learning rate	Number of epochs	Batch size
<b>One-day-ahead</b>	<b>E-2-station</b>					
	AEIO-R-GRU	41	81	0.27	0.7	18

	Model	Window size	Number of hidden units	Dropout rate	Learning rate	Number of epochs	Batch size
<b>displacement prediction</b>	<b>SAA- station</b>						
	AEIO-R-GRU	54	145	0.19	0.46	32	32
<b>Seven-day-ahead of displacement prediction</b>	<b>E-2- station</b>						
	AEIO-R-GRU	97	164	0.24	0.61	20	32
	<b>SAA- station</b>						
	AEIO-R-GRU	69	147	0.28	0.31	17	32

### 619 4.2.3 CNN Models

620 This section presents the results of utilizing CNN models, including VGG, ResNet, Inception,  
621 Xception, DenseNet, and NASNet, to predict deep-seated landslide displacement. The CNN models in  
622 this part use the default settings (Chou and Nguyen, 2023). Table 11 displays the prediction error results  
623 of the CNN models for one-day-ahead and seven-day-ahead forecasts for both E-2 and SAA stations.

624 The prediction results demonstrate that most CNN models produce highly accurate predictions.  
625 Specifically, predictions made by VGG, ResNet, MobileNet, DenseNet, and Inception exhibit MAPE  
626 values below 5%. Among these, MobileNet and DenseNet201 emerge as the two models with the highest  
627 accuracy. For one-day-ahead prediction, the best model for predicting displacement at the E-2 station is  
628 MobileNet, with a MAPE of 4.11%, and the best model for predicting displacement at the SAA station is  
629 DenseNet201, with a MAPE of 6.36%. For seven-day-ahead prediction, the best model for predicting  
630 displacement at the E-2 station is DenseNet201, with a MAPE of 5.3%, and the best model for predicting  
631 displacement at the SAA station is MobileNet, with a MAPE of 6.8%. These models will be selected  
632 accordingly for fine-tuning in the subsequent section.

633 Regarding running time, the CNN models in this section exhibit significantly longer running times  
634 compared to the numerical models in the previous sections. For example, the running time of the best  
635 CNN model to predict one-day-ahead displacement at the E-2 station—MobileNet—is 1.21 hours. In  
636 contrast, the running time of the best single numerical model for predicting this index is 159.97 seconds.

637 While CNN models yield better prediction results, considering their extended running times, users  
638 need to weigh practical considerations before opting for this type of model. For instance, CNN models  
639 should be employed in cases requiring accurate predictions for research and measurement purposes.  
640 Conversely, numerical models like R-GRU are more suitable for real-time predictions and computations  
641 on low-performance devices.

642 Table 11. Performance results of the CNN models for deep-seated displacement prediction

Model	MAPE (%)		MAE (mm)		RMSE (mm)		Time (hour)	
	1-day-ahead	7-day-ahead	1-day-ahead	7-day-ahead	1-day-ahead	7-day-ahead	1-day-ahead	7-day-ahead
<b>E-2- station</b>								
VGG16	4.58	7.38	12.73	13.97	26.54	35.69	3.03	3.31
VGG19	4.47	6.30	12.53	15.11	25.74	32.82	3.14	2.82
ResNet50V2	4.87	7.68	15.28	12.52	31.82	27.19	2.99	3.44
ResNet101V2	4.61	6.60	9.81	9.08	34.67	32.74	2.24	2.96
ResNet152V2	4.71	6.46	7.26	12.60	21.13	19.08	2.94	2.05
InceptionV3	4.99	7.30	11.18	11.65	32.97	34.92	2.43	3.27
InceptionRestNetV2	13.32	15.78	22.51	27.08	76.75	61.11	3.22	3.08
Xception	5.27	7.34	11.60	10.20	35.86	30.68	2.94	3.29
MobileNet	<b>4.11</b>	8.92	12.22	13.62	47.43	31.72	1.21	1.44
DenseNet121	11.15	11.13	16.30	21.49	37.68	46.51	3.32	3.99
DenseNet169	4.74	7.86	11.44	12.20	17.09	36.28	3.02	3.52
DenseNet201	4.66	<b>5.30</b>	8.11	7.44	21.82	10.39	2.09	2.29
NASNetMobile	13.82	15.91	31.00	19.52	46.07	55.65	2.53	3.13
NASNetLarge	13.20	34.23	20.46	61.81	61.52	75.39	3.89	3.93
<b>SAA- station</b>								
VGG16	5.76	7.90	6.07	12.76	9.48	8.95	3.14	3.36
VGG19	5.95	7.32	9.14	13.45	11.68	7.03	3.55	3.20
ResNet50V2	9.87	9.35	12.43	13.81	15.71	9.75	4.57	3.83
ResNet101V2	8.48	17.68	10.56	19.36	11.47	21.94	3.54	3.40
ResNet152V2	9.43	11.42	12.32	10.35	14.91	13.27	3.35	3.88
InceptionV3	10.96	8.11	12.73	9.13	14.48	12.71	3.80	3.18
InceptionRestNetV2	9.86	11.08	13.51	16.75	18.04	21.59	3.23	2.91
Xception	7.42	7.28	7.82	7.08	10.13	10.47	3.48	3.60
MobileNet	7.12	<b>6.80</b>	8.28	9.92	11.58	13.83	1.43	2.13
DenseNet121	8.69	11.69	8.56	14.39	12.54	15.76	3.93	3.42
DenseNet169	6.55	9.56	6.16	9.61	11.08	15.51	3.60	3.76
DenseNet201	<b>6.36</b>	10.45	7.46	11.62	9.37	14.51	2.51	3.13
NASNetMobile	10.31	22.12	13.86	62.04	18.95	43.51	3.56	2.88

Model	MAPE (%)		MAE (mm)		RMSE (mm)		Time (hour)	
	1-day-ahead	7-day-ahead	1-day-ahead	7-day-ahead	1-day-ahead	7-day-ahead	1-day-ahead	7-day-ahead
NASNetLarge	10.25	13.69	11.20	14.05	15.95	19.09	3.18	3.34

#### 643 4.2.4 Best CNN Models Finetuned by AEIO Algorithm

644 In this section, as analyzed in part 4.2.3, the AEIO algorithm will sequentially fine-tune CNN models  
645 to enhance prediction accuracy. Table 12 illustrates the search range of hyperparameters for the CNN  
646 models to be fine-tuned. Table 13 presents the performance results of the CNN models after being fine-  
647 tuned.

648 However, a challenge in this section is that CNN models primarily analyze and learn from image  
649 data. Therefore, numerical data must be converted into image data before training. This poses a challenge  
650 because current computer hardware may need to be fully capable of efficiently converting numerical data  
651 into images for each computation. Hence, this study utilizes the optimal window sizes previously  
652 identified for fine-tuning numerical models (Table 10) for this scenario and employs these fixed window  
653 sizes for CNN models.

654 The results of the fine-tuning process demonstrate that the AEIO has successfully identified the  
655 optimal hyperparameters for the CNN models, enhancing their accuracy. For instance, in the case of the  
656 MobileNet model used for one-day-ahead prediction at the E-2 station, the fine-tuning process reduced  
657 the MAPE of this model from 4.11% to 2.81%. A similar trend is also observed in the remaining prediction  
658 scenarios.

659 Furthermore, similar to the case of AEIO-R-GRU, the CNN models exhibit the same trend, where  
660 one-day-ahead predictions are more accurate than seven-day-ahead predictions. Similarly, forecasts at the  
661 E-2 station demonstrate higher accuracy than predictions at the SAA station. The rationale for this has  
662 been explained in section 4.2.2. Lastly, the optimal hyperparameters of each CNN model, identified by  
663 the AEIO algorithm, are presented in Table 14. CNN models with optimal hyperparameters are the most  
664 effective models in this study for predicting deep-seated displacement.

665 Table 12. Search ranges of the hyperparameters of the optimal hybrid numerical models (Chou and  
666 Nguyen, 2023).

Hybrid model	Hyperparameter	Search range
AEIO-CNN	Learning rate	[0.00, 0.1]
	Decay	[0.00, 0.1]
	Momentum	[0.00, 0.99]

Hybrid model	Hyperparameter	Search range
	Epsilon	[1.0e-7, 0.001]
	Dropout	[0.00, 0.99]
	Epochs	[10, 120]
	Batch size	[32, 64]

667 Table 13. Performance results of best CNN models with AEIO in deep-seated landslide prediction

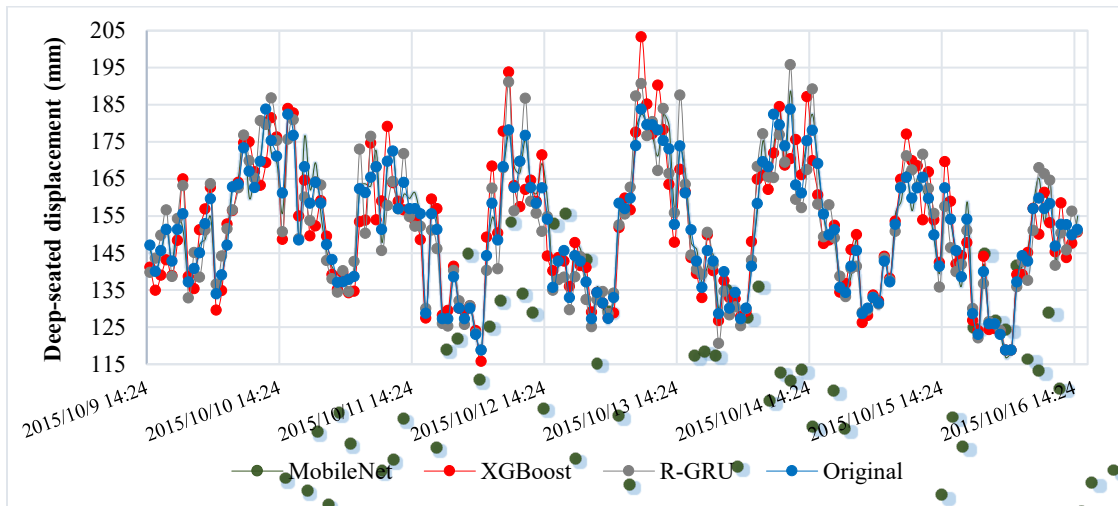
	Model	MAPE (%)	MAE (mm)	RMSE (mm)	Time (hour)
<b>One-day-ahead displacement prediction</b>	<b>E-2-station</b>				
	AEIO-MobileNet	2.81	5.09	11.92	1.25
	<b>SAA-station</b>				
	AEIO-DenseNet201	3.30	6.32	15.65	3.48
<b>Seven-day-ahead of displacement prediction</b>	<b>E-2-station</b>				
	AEIO-DenseNet201	4.30	5.32	15.65	3.48
	<b>SAA-station</b>				
	AEIO-MobileNet	5.63	9.35	14.27	3.39

668

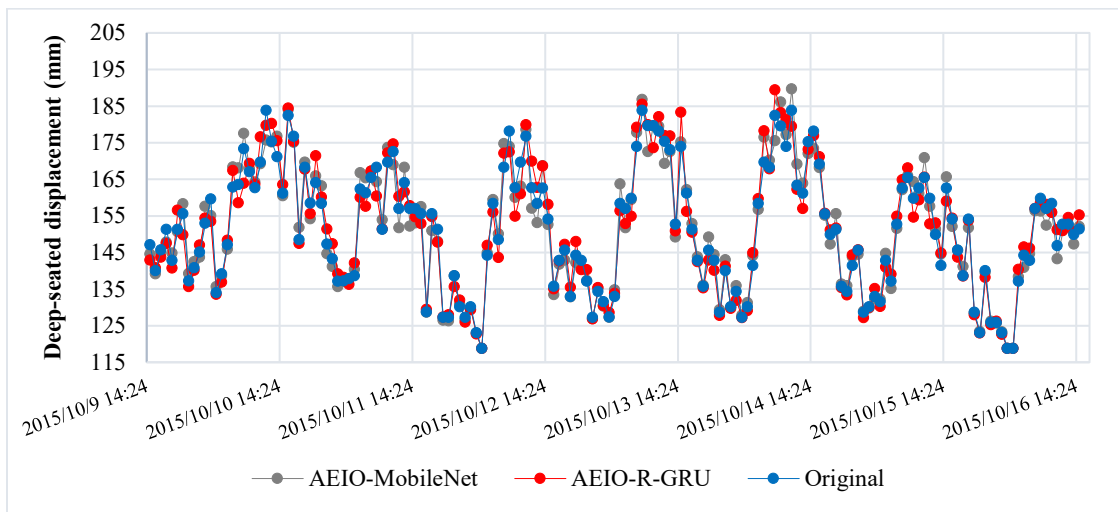
669 Table 14. Optimal hyperparameter of CNN models found by AEIO algorithm

	Model	Learning rate	Decay	Momentum	Epsilon	Dropout	Epochs	Batch size
<b>One-day-ahead displacement prediction</b>	<b>E-2-station</b>							
	AEIO-MobileNet	0.0011	0.00095	0.00001	3.0e-7	0.56	15	64
	<b>SAA-station</b>							
	AEIO-DenseNet201	0.00012	0.0012	0.00011	1.0e-7	0.49	16	64
<b>Seven-day-ahead of displacement prediction</b>	<b>E-2-station</b>							
	AEIO-DenseNet201	0.0012	0.0011	0.00022	1.0e-7	0.51	15	64
	<b>SAA-station</b>							
	AEIO-MobileNet	0.00014	0.00098	0.00011	2.0e-7	0.50	14	64

670 Figure 10 illustrates the differences between typical AI models' actual and predicted deep-seated  
 671 displacement. Specifically, Figure 10a compares the performance of single models against the predicted  
 672 values, while Figure 10b does the same for hybrid models. The chart shows hybrid models demonstrate  
 673 superior predictive capability for deep-seated landslides compared to single models. This is evident from  
 674 the displacement line of the hybrid models in Figure 10b, which closely aligns with the actual deep-seated  
 675 displacement and significantly outperforms the single models depicted in Figure 10a.



676 a) Prediction results of deep-seated displacement by single AI models.  
 677



678 b) Prediction results of deep-seated displacement by AI models optimized using the AEIO algorithm.  
 679

680 Figure 10. Graph comparing the real and predicted deep-seated displacement.

### 681 4.3 Discussion

682 This study centers on landslides in Lushan Mountain, Taiwan, adopting a fundamentally different  
 683 approach than previous research. While past studies primarily focused on constructing AI models for  
 684 classification, calculating the probability of landslide occurrences, and generating landslide susceptibility  
 685 maps (Balogun et al., 2021; Hakim et al., 2022; Jaafari et al., 2022), our study is oriented towards  
 686 predicting displacement to provide warnings about potential landslide hazards.



687 As utilized in our calculations, computing deep-seated displacement offers several benefits. Firstly,  
688 understanding internal displacements provides accurate information for engineers to assess the resilience  
689 of structures and infrastructure in at-risk areas, facilitating the issuance of sensible warnings. Secondly,  
690 forecasting deep-seated displacement offers insights into the severity of the disaster, aiding in effective  
691 evacuation and rescue planning.

692 Moreover, unlike AI models in previous studies (Balogun et al., 2021; Hakim et al., 2022; Jaafari et  
693 al., 2022), our research incorporates machine learning, time series deep learning, and CNN models,  
694 utilizing metaheuristic optimization algorithms to fine-tune their hyperparameters. However, the novelty  
695 of our study lies in adopting pre-trained models, such as MobileNet, DenseNet, Inception, and VGG,  
696 rather than standard CNN models.

697 By employing various AI models, this study identifies the most effective model for predicting deep-  
698 seated landslides and offers a comprehensive overview of the performance of different AI models. Initially,  
699 machine learning models exhibited relatively high prediction errors, with MAPE ranging from 8.14% to  
700 15.19%. This performance was generally lower than time-series deep learning models, which showed  
701 MAPEs ranging from 7.9% to 14.73%. The superior performance of the time series deep learning models  
702 is attributed to their ability to process sequential data and retain information from previous steps. This  
703 enables them to learn patterns from the dataset more effectively than traditional machine learning models.

704 However, compared to CNN models, the results of the time series deep learning models are not as  
705 strong. This disparity is attributed to CNN's superior learning mechanism. The convolutional and pooling  
706 layers in CNN enable robust feature extraction from the input data. Convolutional layers are particularly  
707 effective at identifying complex patterns and subtle features within time series data, primarily when spatial  
708 correlations exist. This capability allows CNN to uncover essential features that other models might  
709 overlook.

710 The models developed in this study demonstrate predictive solid capabilities for deep-seated  
711 displacement. Among them, the AEIO-MobileNet model is the most effective, achieving predictions with  
712 deficient error, indicated by a MAPE of 2.81%. However, these models' practical applicability in real-  
713 world scenarios must be improved due to the time-consuming processes involved in data collection,  
714 processing, and AI model operation, making timely predictions challenging. Meanwhile, there have been  
715 studies that successfully built real-time landslide detection systems (Wang et al., 2023; Das et al., 2020;  
716 C. et al., 2021). We acknowledge this limitation of our study. Therefore, future research endeavors will  
717 aim to address this issue.

718 The input data used for the AI models were selected because they significantly influence the  
719 likelihood of deep-seated landslides, as detailed in Section 3.6. However, a limitation of this study is that  
720 it does not evaluate the relative importance of each input data type on prediction accuracy. Future research

721 should explore the impact of different combinations of input data on AI model performance. This could  
722 help identify the significance of each input type and potentially reveal the optimal combination of inputs  
723 to enhance prediction accuracy further.

## 724 **5. Conclusion**

725 This study addresses the persistent threat of landslides, a primary concern due to their severe impact  
726 on lives and property. Employing various AI models, such as machine learning, time series deep learning,  
727 CNN models, and metaheuristic optimization algorithms, the research focuses on predicting deep-seated  
728 landslides at Lushan Mountain in Ren'ai Township, Nantou County. The study aims to enhance early  
729 prediction accuracy by utilizing eight years of displacement and groundwater level data from Lushan  
730 Mountain and weather data from the POWER project. The predictions cover one-day and seven-day  
731 intervals, serving diverse purposes in landslide forecasting for timely evacuation. The research explores  
732 single and hybrid AI models to determine the most effective approach. The following conclusions are  
733 drawn from this research:

734 (a). CNN models optimized by the novel AEIO algorithm yield the best prediction results. In particular,  
735 AEIO-MobileNet predicts one-day-ahead displacement at the E-2 station with a MAPE score of only  
736 2.81%, demonstrating high accuracy.

737 (b). While CNN models boast high prediction accuracy, their computational time is also considerable.  
738 Therefore, decisions regarding their usage should also consider real-world constraints.

739 (c). The AEIO-R-GRU model also yields reasonably good prediction results, although not on par with  
740 CNN models. The best result achieved by the AEIO-R-GRU model is a MAPE of 3.03% for one-day-  
741 ahead prediction at the E-2 station.

742 (d). The AEIO algorithm has successfully fine-tuned hyperparameters for AI models. Especially in the  
743 case of predicting one-day-ahead displacement, it has aided the MobileNet model in improving its  
744 predictive capability by 31.6%, enabling this model to provide more accurate predictions.

745 (e). The prediction results from the E-2 station consistently outperform those from the SAA station. This  
746 is attributed to the fact that data from the E-2 station has been collected over a longer and more  
747 comprehensive period.

748 (f). The study results demonstrate that AI models can accurately predict deep-seated displacement, which  
749 can be implemented in real-world scenarios.

## 750 **Declare of Competing Interest**

751 The authors declare that there are no known conflicts of interest associated with this publication, and  
752 there has been no significant financial support for this work that could have influenced its outcome.

## 753 **Data Availability Statement**

754 The data and source codes supporting this study's findings are available at  
755 <https://www.researchgate.net/profile/Jui-Sheng-Chou> and from the corresponding author upon reasonable  
756 request.

## 757 **Acknowledgments**

758 The authors thank the National Science and Technology Council (NSTC), Taiwan, for financially  
759 supporting this research under NSTC grants 112-2221-E-011-033-MY3 and 111-2221-E-011-037-MY3.

## 760 **Author contribution**

761 Jui-Sheng Chou: conceptualization, methodology, supervision, writing manuscript, reviewing, and  
762 editing. Hoang-Minh Nguyen: data processing, coding, and writing manuscript. Huy-Phuong Phan: Data  
763 processing, coding, and manuscript writing. Kuo-Lung Wang: data preparation, supervision, and  
764 reviewing.

## 765 **References**

766 Aggarwal, A., Alshehri, M., Kumar, M., Alfarraj, O., Sharma, P., and Pardasani, K. R.: Landslide data  
767 analysis using various time-series forecasting models, *Comput Electr Eng*, 88,  
768 <https://doi.org/10.1016/j.compeleceng.2020.106858>, 2020.

769 Alzubaidi, L., Zhang, J., Humaidi, A. J., Al-Dujaili, A., Duan, Y., Al-Shamma, O., Santamaría, J., Fadhel,  
770 M. A., Al-Amidie, M., and Farhan, L.: Review of deep learning: concepts, CNN architectures, challenges,  
771 applications, future directions, *Journal of Big Data*, 8, 53, <https://doi.org/10.1186/s40537-021-00444-8>,  
772 2021.

773 Balogun, A. L., Rezaie, F., Pham, Q. B., Gigovic, L., Drobnjak, S., Aina, Y. A., Panahi, M., Yekeen, S.  
774 T., and Lee, S.: Spatial prediction of landslide susceptibility in western Serbia using hybrid support vector  
775 regression (SVR) with GWO, BAT and COA algorithms, *Geosci Front*, 12,  
776 <https://doi.org/10.1016/j.gsf.2020.10.009>, 2021.

777 Breiman, L.: *Classification and Regression Trees*, Taylor & Francis Group, New York,  
778 <https://doi.org/10.1201/9781315139470>, 1984.

779 C., P., R., A., Kanwar, V. S., and B., N.: Design and Development of Real-time landslide early warning  
780 system through low cost soil and rainfall sensors, *Materials Today: Proceedings*, 45, 5649-5654,  
781 <https://doi.org/10.1016/j.matpr.2021.02.456>, 2021.

782 Caleca, F., Scaini, C., Frodella, W., and Tofani, V.: Regional-scale landslide risk assessment in Central  
783 Asia, *Nat Hazard Earth Sys*, 24, 13-27, <https://doi.org/10.5194/nhess-24-13-2024>, 2024.

784 Chae, B.-G., Park, H. J., Catani, F., Simoni, A., and Berti, M.: Landslide prediction, monitoring and early  
785 warning: a concise review of state-of-the-art, *Geosciences Journal*, 21, 1033-1070,  
786 <https://doi.org/10.1007/s12303-017-0034-4>, 2017.

787 Chen; T. and Guestrin, C.: XGBoost: A Scalable Tree Boosting System, In *Proceedings of the 22nd ACM*  
788 *SIGKDD International Conference on Knowledge Discovery and Data Mining*, New York, NY, USA,  
789 785–794, <https://doi.org/10.1145/2939672.2939785>, 2016.

790 Chigira, M.: September 2005 rain-induced catastrophic rockslides on slopes affected by deep-seated  
791 gravitational deformations, Kyushu, southern Japan, *Eng Geol*, 108, 1-15,  
792 <https://doi.org/10.1016/j.enggeo.2009.03.005>, 2009.

- 793 Chollet, F.: Xception: Deep Learning with Depthwise Separable Convolutions, 2017 IEEE Conference on  
794 Computer Vision and Pattern Recognition (CVPR), Honolulu, HI, USA, July 21, 2017,  
795 <https://doi.org/10.48550/arXiv.1610.02357>, 2017.
- 796 Chou, J. S. and Ngo, N. T.: Time series analytics using sliding window metaheuristic optimization-based  
797 machine learning system for identifying building energy consumption patterns, *Appl Energ*, 177, 751-770,  
798 <https://doi.org/10.1016/j.apenergy.2016.05.074>, 2016.
- 799 Chou, J. S. and Nguyen, N. Q.: Forecasting Regional Energy Consumption via Jellyfish Search-Optimized  
800 Convolutional-Based Deep Learning, *Int J Energ Res*, Volume 2023,  
801 <https://doi.org/10.1155/2023/3056688>, 2023.
- 802 Corominas, J., van Westen, C., Frattini, P., Cascini, L., Malet, J. P., Fotopoulou, S., Catani, F., Van Den  
803 Eeckhaut, M., Mavrouli, O., Agliardi, F., Pitilakis, K., Winter, M. G., Pastor, M., Ferlisi, S., Tofani, V.,  
804 Hervás, J., and Smith, J. T.: Recommendations for the quantitative analysis of landslide risk, *Bulletin of*  
805 *Engineering Geology and the Environment*, 73, 209-263, <https://doi.org/10.1007/s10064-013-0538-8>,  
806 2014.
- 807 Cotecchia, F., Santaloia, F., and Tagarelli, V.: Towards A Geo-Hydro-Mechanical Characterization of  
808 Landslide Classes: Preliminary Results, *Applied Sciences*, 10, <https://doi.org/10.3390/app10227960>, 2020.
- 809 Crosta, G. B. and Agliardi, F.: Failure forecast for large rock slides by surface displacement measurements,  
810 *Canadian Geotechnical Journal*, 40, 176-191, <https://doi.org/10.1139/t02-085>, 2003.
- 811 Dahal, A., Tanyas, H., Westen, C. v., Meijde, M. v. d., Mai, P. M., Huser, R., and Lombardo, L.: Space–  
812 time landslide hazard modeling via Ensemble Neural Networks, *Nat Hazard Earth Sys*, 24, 823-845,  
813 <https://doi.org/10.5194/nhess-24-823-2024>, 2024.
- 814 Das, K., Majumdar, S., Moulik, S., and Fujita, M.: Real-Time Threshold-based Landslide Prediction  
815 System for Hilly Region using Wireless Sensor Networks, 2020 IEEE International Conference on  
816 Consumer Electronics - Taiwan (ICCE-Taiwan), Taoyuan, Taiwan, [https://doi.org/10.1109/ICCE-  
817 Taiwan49838.2020.9258181](https://doi.org/10.1109/ICCE-Taiwan49838.2020.9258181), 2020.
- 818 Das, S., Sarkar, S., and Kanungo, D. P.: Rainfall-induced landslide (RFIL) disaster in Dima Hasao, Assam,  
819 Northeast India, *Landslides*, 19, 2801-2808, <https://doi.org/10.1007/s10346-022-01962-z>, 2022.
- 820 Di Nunno, F., de Marinis, G., and Granata, F.: Short-term forecasts of streamflow in the UK based on a  
821 novel hybrid artificial intelligence algorithm, *Scientific Reports*, 13, 7036,  
822 <https://doi.org/10.1038/s41598-023-34316-3>, 2023.
- 823 Drucker, H., Burges, C. J. C., Kaufman, L., Smola, A., and Vapnik, V.: Support vector regression  
824 machines, *NIPS'96: Proceedings of the 9th International Conference on Neural Information Processing*  
825 *Systems*, 155-161, 1996.
- 826 Elman, J. L.: Finding Structure in Time, *Cognitive Sci*, 14, 179-211, [https://doi.org/10.1016/0364-  
827 0213\(90\)90002-E](https://doi.org/10.1016/0364-0213(90)90002-E), 1990.
- 828 Fu, W. X. and Liao, Y.: Non-linear shear strength reduction technique in slope stability calculation,  
829 *Comput Geotech*, 37, 288-298, <https://doi.org/10.1016/j.compgeo.2009.11.002>, 2010.
- 830 Geertsema, M., Hungr, O., Schwab, J. W., and Evans, S. G.: A large rockslide-debris avalanche in  
831 cohesive soil at Pink Mountain, northeastern British Columbia, Canada, *Eng Geol*, 83, 64-75,  
832 <https://doi.org/10.1016/j.enggeo.2005.06.025>, 2006.
- 833 Hakim, W. L., Rezaie, F., Nur, A. S., Panahi, M., Khosravi, K., Lee, C. W., and Lee, S.: Convolutional  
834 neural network (CNN) with metaheuristic optimization algorithms for landslide susceptibility mapping in  
835 Icheon, South Korea, *J Environ Manage*, 305, <https://doi.org/10.1016/j.jenvman.2021.114367>, 2022.

- 836 Han, H. G., Chen, Q. L., and Qiao, J. F.: Research on an online self-organizing radial basis function neural  
837 network, *Neural Comput Appl*, 19, 667-676, <https://doi.org/10.1007/s00521-009-0323-6>, 2010.
- 838 Han, J., Kamber, M., and Pei, J.: *Data Mining: Concepts and Techniques*, Southeast Asia Edition, Morgan  
839 Kaufmann Publishers Inc., San Francisco, CA, United States, 696 pp., <https://doi.org/10.1016/C2009-0-61819-5>, 2006.
- 841 He, K., Zhang, X., Ren, S., and Sun, J.: Deep Residual Learning for Image Recognition, 2016 IEEE  
842 Conference on Computer Vision and Pattern Recognition, <https://doi.org/10.48550/arXiv.1512.03385>,  
843 2016.
- 844 He, R., Zhang, W., Dou, J., Jiang, N., Xiao, H., and Zhou, J.: Application of artificial intelligence in three  
845 aspects of landslide risk assessment: A comprehensive review, *Rock Mechanics Bulletin*,  
846 <https://doi.org/https://doi.org/10.1016/j.rockmb.2024.100144>, 2024.
- 847 Howard, A. G., Zhu, M., Chen, B., Kalenichenko, D., Wang, W., Weyand, T., Andreetto, M., and Adam,  
848 H.: MobileNets: Efficient Convolutional Neural Networks for Mobile Vision Applications, *CoRR*,  
849 abs/1704.04861, <https://doi.org/10.48550/arXiv.1704.04861>, 2017.
- 850 Hu, B., Su, G., Jiang, J., Sheng, J., and Li, J.: Uncertain Prediction for Slope Displacement Time-Series  
851 Using Gaussian Process Machine Learning, *Ieee Access*, PP, 1-1,  
852 <https://doi.org/10.1109/ACCESS.2019.2894807>, 2019.
- 853 Hu, X. L., Wu, S. S., Zhang, G. C., Zheng, W. B., Liu, C., He, C. C., Liu, Z. X., Guo, X. Y., and Zhang,  
854 H.: Landslide displacement prediction using kinematics-based random forests method: A case study in  
855 Jinping Reservoir Area, China, *Eng Geol*, 283, <https://doi.org/10.1016/j.enggeo.2020.105975>, 2021.
- 856 Huang, G., Liu, Z., Maaten, L. v. d., and Weinberger, K. Q.: Densely Connected Convolutional Networks,  
857 2017 IEEE Conference on Computer Vision and Pattern Recognition (CVPR),  
858 <https://doi.org/10.1109/CVPR.2017.243>, 2017.
- 859 Huang, R. Q. and Fan, X. M.: The landslide story, *Nat Geosci*, 6, 325-326,  
860 <https://doi.org/10.1038/ngeo1806>, 2013.
- 861 Hungr, O., Leroueil, S., and Picarelli, L.: The Varnes classification of landslide types, an update,  
862 *Landslides*, 11, 167-194, <https://doi.org/10.1007/s10346-013-0436-y>, 2014.
- 863 Jaafari, A., Jaafari, A., Panahi, M., Panahi, M., Mafi-Gholami, D., Mafi-Gholami, D., Rahmati, O.,  
864 Rahmati, O., Shahabi, H., Shahabi, H., Shirzadi, A., Shirzadi, A., Lee, S., Lee, S., Bui, D. T., Bui, D. T.,  
865 Pradhan, B., and Pradhan, B.: Swarm intelligence optimization of the group method of data handling using  
866 the cuckoo search and whale optimization algorithms to model and predict landslides, *Appl Soft Comput*,  
867 116, <https://doi.org/10.1016/j.asoc.2021.108254>, 2022.
- 868 Jiang, J., Ehret, D., Xiang, W., Rohn, J., Huang, L., Yan, S., and Bi, R.: Numerical simulation of Qiaotou  
869 Landslide deformation caused by drawdown of the Three Gorges Reservoir, China, *Environmental Earth  
870 Sciences*, 62, 411-419, <https://doi.org/10.1007/s12665-010-0536-0>, 2011.
- 871 Jones, J. N., Bennett, G. L., Abanco, C., Matera, M. A. M., and Tan, F. J.: Multi-event assessment of  
872 typhoon-triggered landslide susceptibility in the Philippines, *Nat Hazard Earth Sys*, 23, 1095-1115,  
873 <https://doi.org/10.5194/nhess-23-1095-2023>, 2023.
- 874 Keqiang, H., Zhiliang, W., Xiaoyun, M., and Zengtao, L.: Research on the displacement response ratio of  
875 groundwater dynamic augment and its application in evaluation of the slope stability, *Environmental Earth  
876 Sciences*, 74, 5773-5791, <https://doi.org/10.1007/s12665-015-4595-0>, 2015.
- 877 Kilburn, C. R. J. and Petley, D. N.: Forecasting giant, catastrophic slope collapse: lessons from Vajont,  
878 Northern Italy, *Geomorphology*, 54, 21-32, [https://doi.org/10.1016/S0169-555x\(03\)00052-7](https://doi.org/10.1016/S0169-555x(03)00052-7), 2003.

879 Kumar, D., Ikhwan, N., and Rawat, A.: Study and Prediction of Landslide in Uttarkashi, Uttarakhand,  
880 India Using GIS and ANN, American Journal of Neural Networks and Applications 3,  
881 <https://doi.org/10.11648/j.ajna.20170306.12>, 2017.

882 Lau, Y. M., Wang, K. L., Wang, Y. H., Yiu, W. H., Ooi, G. H., Tan, P. S., Wu, J., Leung, M. L., Lui, H.  
883 L., and Chen, C. W.: Monitoring of rainfall-induced landslides at Songmao and Lushan, Taiwan, using  
884 IoT and big data-based monitoring system, Landslides, 20, 271-296, <https://doi.org/10.1007/s10346-022-01964-x>, 2023.

886 Lee, Y. F. and Chi, Y. Y.: Rainfall-induced landslide risk at Lushan, Taiwan, Eng Geol, 123, 113-121,  
887 <https://doi.org/10.1016/j.enggeo.2011.03.006>, 2011.

888 Li, H., Xu, Q., He, Y., and Deng, J.: Prediction of landslide displacement with an ensemble-based extreme  
889 learning machine and copula models, Landslides, 15, 2047-2059, <https://doi.org/10.1007/s10346-018-1020-2>, 2018.

891 Lin, C. W., Tseng, C. M., Tseng, Y. H., Fei, L. Y., Hsieh, Y. C., and Tarolli, P.: Recognition of large scale  
892 deep-seated landslides in forest areas of Taiwan using high resolution topography, J Asian Earth Sci, 62,  
893 389-400, <https://doi.org/10.1016/j.jseaes.2012.10.022>, 2013.

894 Lin, H. H., Lin, M. L., Lu, J. H., Chi, C. C., and Fei, L. Y.: Deep-seated gravitational slope deformation  
895 in Lushan, Taiwan: Transformation from cleavage-controlled to weakened rockmass-controlled  
896 deformation, Eng Geol, 264, <https://doi.org/10.1016/j.enggeo.2019.105387>, 2020.

897 Liu, C. Y., Jiang, Z. S., Han, X. S., and Zhou, W. X.: Slope displacement prediction using sequential  
898 intelligent computing algorithms, Measurement, 134, 634-648,  
899 <https://doi.org/10.1016/j.measurement.2018.10.094>, 2019.

900 Loche, M. and Scaringi, G.: Temperature and shear-rate effects in two pure clays: Possible implications  
901 for clay landslides, Results Eng, 20, <https://doi.org/10.1016/j.rineng.2023.101647>, 2023.

902 Margarint, M. C., Grozavu, A., and Patriche, C. V.: Assessing the spatial variability of coefficients of  
903 landslide predictors in different regions of Romania using logistic regression, Nat Hazard Earth Sys, 13,  
904 3339-3355, <https://doi.org/10.5194/nhess-13-3339-2013>, 2013.

905 Matsushi, Y. and Matsukura, Y.: Rainfall thresholds for shallow landsliding derived from pressure-head  
906 monitoring: cases with permeable and impermeable bedrocks in Boso Peninsula, Japan, Earth Surf Proc  
907 Land, 32, 1308-1322, <https://doi.org/10.1002/esp.1491>, 2007.

908 McCulloch, W. and Pitts, A.: A Logical Calculus of the Ideas Immanent in Nervous Activity (1943), Ideas  
909 That Created the Future, 79-88, <https://doi.org/10.1007/BF02478259>, 2021.

910 Miao, H. B. and Wang, G. H.: Prediction of landslide velocity and displacement from groundwater level  
911 changes considering the shear rate-dependent friction of sliding zone soil, Eng Geol, 327,  
912 <https://doi.org/10.1016/j.enggeo.2023.107361>, 2023.

913 Millán-Arancibia, C. and Lavado-Casimiro, W.: Rainfall thresholds estimation for shallow landslides in  
914 Peru from gridded daily data, Nat Hazard Earth Sys, 23, 1191-1206, <https://doi.org/10.5194/nhess-23-1191-2023>, 2023.

916 Mufundirwa, A., Fujii, Y., and Kodama, J.: A new practical method for prediction of geomechanical  
917 failure-time, Int J Rock Mech Min, 47, 1079-1090, <https://doi.org/10.1016/j.ijrmms.2010.07.001>, 2010.

918 Perkins, J. P., Oakley, N. S., Collins, B. D., Corbett, S. C., and Burgess, W. P.: Characterizing the scale  
919 of regional landslide triggering from storm hydrometeorology, Nat Hazard Earth Sys,  
920 <https://doi.org/10.5194/egusphere-2024-873>, 2024.



921 Peternel, T., Janža, M., Šegina, E., Bezak, N., and Maček, M.: Recognition of Landslide Triggering  
922 Mechanisms and Dynamics Using GNSS, UAV Photogrammetry and In Situ Monitoring Data, Remote  
923 Sensing, 14, <https://doi.org/10.3390/rs14143277>, 2022.

924 Petley, D.: Global patterns of loss of life from landslides, *Geology*, 40, 927-930,  
925 <https://doi.org/10.1130/G33217.1>, 2012.

926 Petley, D. N., Mantovani, F., Bulmer, M. H., and Zannoni, A.: The use of surface monitoring data for the  
927 interpretation of landslide movement patterns, *Geomorphology*, 66, 133-147,  
928 <https://doi.org/10.1016/j.geomorph.2004.09.011>, 2005.

929 Pham, B. T., Pradhan, B., Bui, D. T., Prakash, I., and Dholakia, M. B.: A comparative study of different  
930 machine learning methods for landslide susceptibility assessment: A case study of Uttarakhand area  
931 (India), *Environ Modell Softw*, 84, 240-250, <https://doi.org/10.1016/j.envsoft.2016.07.005>, 2016.

932 Pinyol, N. M., Alvarado, M., Alonso, E. E., and Zabala, F.: Thermal effects in landslide mobility,  
933 *Geotechnique*, 68, 528-545, <https://doi.org/10.1680/jgeot.17.P.054>, 2018.

934 Preisig, G.: Forecasting the long-term activity of deep-seated landslides via groundwater flow and slope  
935 stability modelling, *Landslides*, 17, 1693-1702, <https://doi.org/10.1007/s10346-020-01427-1>, 2020.

936 Ruitang, L., Zhaowei, C., Zexiong, W., Zhenghan, Z., Jiahao, L., Zhencheng, G., and Yuchong, C.:  
937 Mountain Slope Monitoring Guidelines (TGS-SLOPEM106), 2017.

938 Shibasaki, T., Matsuura, S., and Hasegawa, Y.: Temperature-dependent residual shear strength  
939 characteristics of smectite-bearing landslide soils, *J Geophys Res-Sol Ea*, 122, 1449-1469,  
940 <https://doi.org/10.1002/2016jb013241>, 2017.

941 Simonyan, K. and Zisserman, A.: Very Deep Convolutional Networks for Large-Scale Image Recognition,  
942 *ICLR2015*, <https://doi.org/10.48550/arXiv.1409.1556>, 2015.

943 Srivastava, S., Anand, N., Sharma, S., Dhar, S., and Sinha, L. K.: Monthly Rainfall Prediction Using  
944 Various Machine Learning Algorithms for Early Warning of Landslide Occurrence, 2020 International  
945 Conference for Emerging Technology (INCET), Belgaum, India, 5-7 June 2020, 1-7,  
946 <https://doi.org/10.1109/INCET49848.2020.9154184>, 2020.

947 Stanton, J. M.: Galton, Pearson, and the Peas: A Brief History of Linear Regression for Statistics  
948 Instructors, *Journal of Statistics Education*, 9, <https://doi.org/10.1080/10691898.2001.11910537>, 2001.

949 Szegedy, C., Vanhoucke, V., Ioffe, S., Shlens, J., and Wojna, Z.: Rethinking the Inception Architecture  
950 for Computer Vision, 2016 IEEE Conference on Computer Vision and Pattern Recognition (CVPR), 2818-  
951 2826, <https://doi.org/https://doi.org/10.1109/CVPR.2016.308>, 2015.

952 Take, W. A., Beddoe, R. A., Davoodi-Bilesavar, R., and Phillips, R.: Effect of antecedent groundwater  
953 conditions on the triggering of static liquefaction landslides, *Landslides*, 12, 469-479,  
954 <https://doi.org/10.1007/s10346-014-0496-7>, 2015.

955 Thai Pham, B., Shirzadi, A., Shahabi, H., Omidvar, E., Singh, S. K., Sahana, M., Talebpour Asl, D., Bin  
956 Ahmad, B., Kim Quoc, N., and Lee, S.: Landslide Susceptibility Assessment by Novel Hybrid Machine  
957 Learning Algorithms, *Sustainability-Basel*, 11, <https://doi.org/10.3390/su11164386>, 2019.

958 van Natijne, A. L., Bogaard, T. A., Zieher, T., Pfeiffer, J., and Lindenbergh, R. C.: Machine-learning-  
959 based nowcasting of the Vögelsberg deep-seated landslide: why predicting slow deformation is not so  
960 easy, *Nat Hazard Earth Sys*, 23, 3723-3745, <https://doi.org/10.5194/nhess-23-3723-2023>, 2023.

961 Wang, K.-L., Lin, M.-L., Lin, J.-T., Huang, S.-C., Liao, R.-T., and Chen, C.-W.: Monitoring of the  
962 Evolution of a Deep-Seated Landslide in Lushan Area, Taiwan, *Engineering Geology for Society and  
963 Territory*, 2, 1317-1320, [https://doi.org/https://doi.org/10.1007/978-3-319-09057-3\\_231](https://doi.org/https://doi.org/10.1007/978-3-319-09057-3_231), 2015.

- 964 Wang, Y., Dong, J., Zhang, L., Deng, S. H., Zhang, G. K., Liao, M. S., and Gong, J. Y.: Automatic  
965 detection and update of landslide inventory before and after impoundments at the Lianghekou reservoir  
966 using Sentinel-1 InSAR, *Int J Appl Earth Obs*, 118, <https://doi.org/10.1016/j.jag.2023.103224>, 2023.
- 967 Wu, J. H.: Seismic landslide simulations in discontinuous deformation analysis, *Comput Geotech*, 37,  
968 594-601, <https://doi.org/10.1016/j.compgeo.2010.03.007>, 2010.
- 969 Xu, J., Jiang, Y., and Yang, C.: Landslide Displacement Prediction during the Sliding Process Using  
970 XGBoost, SVR and RNNs, *Applied Sciences*, 12, <https://doi.org/10.3390/app12126056>, 2022.
- 971 Xu, J., Li, H., Du, K., Yan, C., Zhao, X., Li, W., and Xu, X.: Field investigation of force and displacement  
972 within a strata slope using a real-time remote monitoring system, *Environmental Earth Sciences*, 77, 552,  
973 <https://doi.org/10.1007/s12665-018-7729-3>, 2018.
- 974 Yang, B., Yin, K., Lacasse, S., and Liu, Z.: Time series analysis and long short-term memory neural  
975 network to predict landslide displacement, *Landslides*, 16, <https://doi.org/10.1007/s10346-018-01127-x>,  
976 2019.
- 977 Yang, S., Jin, A., Nie, W., Liu, C., and Li, Y.: Research on SSA-LSTM-Based Slope Monitoring and  
978 Early Warning Model, *Sustainability-Basel*, 14, <https://doi.org/10.3390/su141610246>, 2022.
- 979 Zhang, L., Shi, B., Zhu, H., Yu, X. B., Han, H., and Fan, X.: PSO-SVM-based deep displacement  
980 prediction of Majiagou landslide considering the deformation hysteresis effect, *Landslides*, 18, 179-193,  
981 <https://doi.org/10.1007/s10346-020-01426-2>, 2021.
- 982 Zhang, W., Li, H., Tang, L., Gu, X., Wang, L., and Wang, L.: Displacement prediction of Jiuxianping  
983 landslide using gated recurrent unit (GRU) networks, *Acta Geotechnica*, 17, 1367-1382,  
984 <https://doi.org/10.1007/s11440-022-01495-8>, 2022.
- 985 Zhang, W. G., Zhang, R. H., Wu, C. Z., Goh, A. T. C., Lacasse, S., Liu, Z. Q., and Liu, H. L.: State-of-  
986 the-art review of soft computing applications in underground excavations, *Geosci Front*, 11, 1095-1106,  
987 <https://doi.org/10.1016/j.gsf.2019.12.003>, 2020.
- 988 Zheng, H. Y., Liu, B., Han, S. Y., Fan, X. Y., Zou, T. Y., Zhou, Z. L., and Gong, H.: Research on landslide  
989 hazard spatial prediction models based on deep neural networks: a case study of northwest Sichuan, China,  
990 *Environmental Earth Sciences*, 81, <https://doi.org/10.1007/s12665-022-10369-x>, 2022.
- 991 Zhou, C., Yin, K., Cao, Y., Ahmed, B., and Fu, X.: A novel method for landslide displacement prediction  
992 by integrating advanced computational intelligence algorithms, *Scientific Reports*, 8, 7287,  
993 <https://doi.org/10.1038/s41598-018-25567-6>, 2018.
- 994 Zoph, B., Vasudevan, V., Shlens, J., and Le, Q. V.: Learning Transferable Architectures for Scalable  
995 Image Recognition, 2018 IEEE/CVF Conference on Computer Vision and Pattern Recognition (CVPR),  
996 8697-8710, <https://doi.org/10.1109/CVPR.2018.00907>, 2018.
- 997